J. Fluid Mech. (2008), *vol.* 597, *pp.* 1–29.
doi:10.1017/S0022112007009639 Printed in the United Kingdom

Wake transition in the flow around two circular cylinders in staggered arrangements

BRUNO S. CARMO, SPENCER J. SHERWIN, PETER W. BEARMAN AND RICHARD H. J. WILLDEN

Department of Aeronautics, Imperial College London, South Kensington Campus, London, SW7 2AZ, UK

(Received 24 May 2007 and in revised form 26 September 2007)

The wake transition of the flow around two circular cylinders placed in staggered arrangements with fixed streamwise separation of $5D$ and cross-stream separation varying from 0 to $3D$ has been studied. The wake transition is compared to that of a single isolated cylinder. Linear stability analysis utilizing Floquet theory and direct numerical simulations using a spectral/hp element spatial discretization were carried out. The unstable modes that first appear in the wake transition of the flow around a single cylinder, which are the long-spanwise-wavelength mode A and the short-spanwise-wavelength mode B, are also found in the flow around the staggered arrangements. However, a third mode, referred to as mode C, is also present in the wake transition of the flow around staggered arrangements, depending on the relative positioning of the cylinders. This mode has an intermediate spanwise wavelength and period-doubling character. The structure and onset characteristics of mode C are analysed and the nonlinear character of the bifurcation for this mode is investigated.

1. Introduction

The flow around circular cylinders has been extensively studied owing to its practical importance in engineering and scientific relevance in fluid mechanics. On the engineering side, there are a number of applications in mechanical, civil and naval engineering that employ circular-cylindrical structures, such as heat exchangers, chimneys and offshore platforms. In scientific terms, the flow around circular cylinders presents various important physical phenomena, such as separation, vortex shedding and transition.

In the next two subsections, some of the relevant research that has been carried out on two different aspects of this flow is reviewed. These aspects are the wake transition in bluff body flows and the flow around circular cylinders in staggered arrangements, illustrated in figure 1.

1.1. *Secondary instabilities in the wake*

In the last two decades, much effort has focused on the study of the three-dimensional transition that takes place in the von Kármán wake that appears in the flow downstream of a single cylinder. This line of research in its contemporary form was instigated by the seminal work of Williamson (1988), in which two distinct stages were identified in the wake transition, spanning $160 \lesssim Re \lesssim 300$. The limits of these stages were identified by discontinuities in the curve obtained when the Strouhal number (St) was plotted against the Reynolds number (Re) and these discontinuities correspond to the manifestation of different three-dimensional structures in the wake. The first to appear is called mode A, and it has a spanwise wavelength of

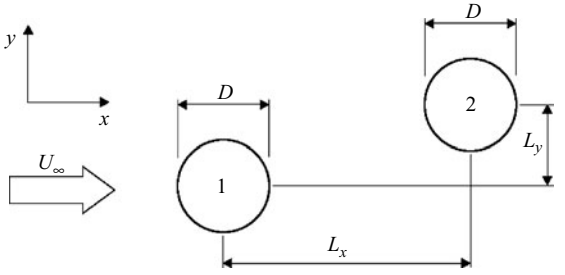

FIGURE 1. Schematic drawing of two circular cylinders in a staggered arrangement.

approximately 4 diameters. The second is called mode B, and its spanwise wavelength is close to 1 diameter. A number of papers on additional experiments and direct numerical simulations (DNS) for this Reynolds number range have been published since then with the aim of reproducing these findings, see for example Wu *et al.* (1994), Zhang *et al.* (1995) and Thompson, Hourigan & Sheridan (1996). A great leap forward occurred with the work of Barkley & Henderson (1996), who performed high-accuracy Floquet stability analyses of two-dimensional time-periodic base flows, precisely identifying the critical Reynolds numbers and also characterizing each of the modes that take part in the wake transition. Williamson (1996) presented an extensive study on the wake transition, setting the most significant results presented so far against some new experimental data in order to show the different symmetries of the modes and to put forward physical mechanisms to explain the origin of the instabilities. He proposed that mode A originates from a elliptic instability in the near-wake vortex cores, while mode B is a manifestation of a hyperbolic instability in the braid shear layers. The research on the physical mechanisms of modes A and B was extended in Leweke & Williamson (1998) and Thompson, Leweke & Williamson (2001). The nonlinear characterization of the bifurcations through which the wake becomes three-dimensional was first assessed by Henderson & Barkley (1996), who found that mode A became unstable through a subcritical bifurcation. This work was extended by Henderson (1997), where it was concluded that mode B bifurcated through a supercritical route. Various other computational papers have expanded the research on the nonlinear features of the first stages of the wake transition, see for instance Persillon & Braza (1998) and Posdziech & Grundmann (2001).

Techniques similar to that presented in Barkley & Henderson (1996) have been used to perform Floquet stability analysis of the flow around other bluff bodies. Robichaux, Balachandar & Vanka (1999) analysed the stability of the wake of the flow around a square cylinder, and found that, besides modes A and B, the geometrical configuration they used presented a third mode of intermediate wavelength, which was called mode S. The authors suggested that this was a period-doubling bifurcation, i.e. an instability whose Floquet multiplier is real and negative. Later, however, Blackburn & Lopez (2003) showed that this was in fact a quasi-periodic mode (the Floquet multiplier is complex), and that the mistake was due to the method used in Robichaux *et al.* (1999), which only allowed the identification of the real part of the Floquet multiplier. This quasi-periodic mode, known as mode QP, was also observed in the wake of a circular cylinder in Blackburn & Lopez (2003) and Barkley & Henderson (1996), but it was stable in the Reynolds number range investigated. Later, Blackburn, Marques & Lopez (2005) presented results of Floquet stability analysis of the flow around a single cylinder carried out for higher Reynolds numbers, and showed that

the mode QP becomes unstable for $Re \approx 377$. Marques, Lopez & Blackburn (2004), using bifurcation theory, showed that only three modes, modes A, B and QP, could possibly be observed in a two-dimensional time-periodic wake with a spatio-temporal symmetry $\mathscr{H}$:

$$\mathscr{H}(u, v)(x, y, t) = (u, -v)\left(x, -y, t + \tfrac{1}{2}T\right)$$

where u and v are the x and y velocity components and T is the period of the wake.

However, for bluff body wakes that do not present this symmetry, a period-doubling mode has also been found. As far as we are aware, the first evidence of this period-doubling mode, which is commonly called mode C, appears in the computations and experiments in Zhang *et al.* (1995) when a tiny trip wire was placed close to a circular cylinder. More recently Sheard, Thompson & Hourigan (2003) identified this mode in the flow around bluff rings by means of Floquet stability calculations. This was extended in Sheard, Thompson & Hourigan (2004), in which a nonlinear characterization of mode C was made by means of DNS. Subsequently, additional computational results were compared to experimental data in Sheard *et al.* (2005*b*) and, more recently, in Sheard, Thompson & Hourigan (2005*a*) a physical mechanism to explain how the mode C instability is sustained has been suggested.

1.2. *The flow around circular cylinders in staggered arrangements*

An important aspect of the flow around bluff bodies such as circular cylinders is that, if two or more bodies are placed in close proximity in the fluid stream, the flow field and fluid loads change dramatically compared to the flow around an isolated body. This phenomenon is known as flow interference. Comparatively few papers on the flow around groups of cylinders have been published, despite the fact that in all the applications cited at the beginning of this section it is common to have circular-cylindrical structures grouped together. The usual approach is to consider only a pair of cylinders of equal diameter, since in such configurations the number of parameters is kept sufficiently low for a proper systematic analysis and the basics of the interference mechanisms can be more easily understood.

An example of this can be found in Zdravkovich (1977), in which an extensive review of flow interference between two circular cylinders in tandem, side-by-side and staggered arrangements was conducted. For all these configurations, discussions about pressure distributions, velocity profiles, flow regimes and patterns, drag and lift forces and Reynolds number effects were presented. In relation to staggered arrangements, Zdravkovich (1977) investigated the physical origin of the non-zero lift forces that are observed for these configurations. Later, Sumner, Price & Païdoussis (2000) put forward a taxonomy for the flow regimes observed in their experiments with staggered arrangements. Based on flow visualization and force measurements, nine different patterns were identified according to the relative position of the cylinders. This work was extended by Akbari & Price (2005), who reproduced the flow regimes using computational simulations and scrutinized the physical features observed in each.

As far as we are aware, no computational work addressing the three-dimensional aspects of the flow around staggered arrangements of circular cylinders has yet been published. This paper focuses on the changes that occur in the transition in the wake when the flow around staggered arrangements is compared to the flow around a single cylinder. The instabilities that arise at the beginning of the transition are characterized by means of linear stability analysis of two-dimensional periodic base flows and also fully three-dimensional simulations.

The paper is organized as follows. In § 2, the numerical methods used to calculate the base flows and their stability are described. Details of the parameters used in the simulations are given in § 3, and in § 4 the results are presented and analysed. Finally, in § 5, conclusions are drawn regarding the effect of the relative position of the cylinders on the three-dimensional bifurcation scenario.

2. Overview

The methodology adopted in this paper can be divided into three distinct parts. The first refers to simulations of two-dimensional time-dependent flows by means of numerical solution of the incompressible Navier–Stokes equations. The second comprises stability calculations of two-dimensional time-periodic flows with respect to three-dimensional perturbations, and this is achieved using Floquet theory. Finally, the third part consists of three-dimensional simulations of selected cases, in order to analyse the nonlinear behaviour of some of the bifurcations found. In the next three subsections, an overview of the mathematical formulation and computational implementation of each of these techniques is provided.

2.1. *Two-dimensional base flow calculation*

We consider a two-dimensional incompressible viscous flow, which is governed by the Navier–Stokes equations. These equations can be written in non-dimensional form using the cylinder diameter D as the reference length and the free-stream flow speed U_∞ as the reference speed:

$$\frac{\partial \boldsymbol{u}}{\partial t} = -(\boldsymbol{u}\cdot\nabla)\boldsymbol{u} - \nabla p + \frac{1}{Re}\nabla^2\boldsymbol{u}, \tag{2.1}$$

$$\nabla\cdot\boldsymbol{u} = 0, \tag{2.2}$$

where $\boldsymbol{u}\equiv(u, v, w)$ is the velocity field, t is the time, p is the static pressure and $Re = U_\infty D/\nu$ is the Reynolds number, where ν is the kinematic viscosity. The pressure is assumed to be scaled by the constant density ρ.

These equations were discretized following the Spectral/hp method as described in Karniadakis & Sherwin (2005). To generate the base flows, equations (2.1) and (2.2) were solved in two dimensions, using a stiffly stable splitting scheme (Karniadakis, Israeli & Orszag 1991).

2.2. *Floquet stability analysis*

For this part, a similar approach to that utilized in Barkley & Henderson (1996) was used. We considered periodic two-dimensional base flows $\boldsymbol{U}(x, y, t)$, with period T, and investigated their stability with respect to an infinitesimal three-dimensional perturbation $\boldsymbol{u}'(x, y, z, t)$. The equations that govern the perturbation evolution to leading order are the linearized Navier–Stokes equations:

$$\frac{\partial \boldsymbol{u}'}{\partial t} = -(\boldsymbol{U}\cdot\nabla)\boldsymbol{u}' - (\boldsymbol{u}'\cdot\nabla)\boldsymbol{U} - \nabla p' + \frac{1}{Re}\nabla^2\boldsymbol{u}', \tag{2.3}$$

$$\nabla\cdot\boldsymbol{u}' = 0, \tag{2.4}$$

where $p'(x, y, z, t)$ is the pressure perturbation. The velocity boundary conditions that were imposed on this system are $\boldsymbol{u}' = 0$ on boundaries where Dirichlet conditions are specified for the base flow, and $\partial\boldsymbol{u}'/\partial\boldsymbol{n} = 0$ on boundaries where Neumann conditions are specified for the base flow.

The right-hand side of (2.3) subjected to the incompressibility constraint of equation (2.4) can be represented by an operator $\boldsymbol{L}$, so we can write the evolution equation in

the compact form:

$$\frac{\partial \boldsymbol{u}'}{\partial t} = \boldsymbol{L}(\boldsymbol{u}'). \tag{2.5}$$

The operator $\boldsymbol{L}(\boldsymbol{u}')$ is T-periodic because it depends linearly on the base flow $\boldsymbol{U}(x, y, t)$, which is T-periodic. Therefore, the stability of (2.5) can be investigated using Floquet analysis. The solutions of (2.5) can be decomposed into a sum of solutions of the form $\tilde{\boldsymbol{u}}(x, y, z, t)\mathrm{e}^{\sigma t}$, where $\tilde{\boldsymbol{u}}(x, y, z, t)$, which are called Floquet modes, are T-periodic solutions. The complex exponents σ are the Floquet exponents, and the sign of their real parts determines the stability of the system. However, in Floquet-type problems it is more usual to consider the Floquet multiplier $\mu \equiv \mathrm{e}^{\sigma T}$ instead of the Floquet exponent. If the Floquet multiplier is located inside the unit circle ($|\mu| < 1$), then the solution will decay exponentially with time, and if the multiplier is located outside the unit circle ($|\mu| > 1$), the solution will grow exponentially with time, rendering the system unstable.

If we consider a system that is homogeneous in the spanwise direction z, a further simplification can be made. A perturbation of the velocity field can be expressed in terms of the Fourier integral:

$$\boldsymbol{u}'(x, y, z, t) = \int_{-\infty}^{\infty} \hat{\boldsymbol{u}}(x, y, \beta, t)\mathrm{e}^{\mathrm{i}\beta z}\mathrm{d}\beta \tag{2.6}$$

and similarly for p'. Since equation (2.5) is linear, modes with different β do not couple. Moreover, because the base flow z-velocity component is zero, perturbations of the form

$$\boldsymbol{u}'(x, y, z, t) = (\hat{u}\cos\beta z, \hat{v}\cos\beta z, \hat{w}\sin\beta z), \tag{2.7}$$

$$p'(x, y, z, t) = \hat{p}\cos\beta z \tag{2.8}$$

remain of this form under the operator $\boldsymbol{L}$. Thus, the Floquet modes $\tilde{\boldsymbol{u}}(x, y, z, t)$ will necessarily be of this form. The expressions (2.7) and (2.8) are appropriate to represent a Floquet mode corresponding to a real Floquet multiplier. However, if the multiplier is complex (as in the case of the QP mode in Blackburn & Lopez 2003) then a Fourier mode containing both real and imaginary components is necessary to represent the Floquet mode. As the velocity components $(\hat{u}, \hat{v}, \hat{w})$ and pressure $\hat{p}$ depend only on x, y and t, the three-dimensional stability problem can be reduced to a series of two-dimensional stability problems, each with a different value of β. Consequently, the stability of such two-dimensional incompressible periodic flows to three-dimensional perturbations can be analysed by computing the Floquet multipliers and corresponding modes as a function of Re and β. Details on how the Floquet multipliers and modes were calculated are given in the Appendix.

2.3. *Three-dimensional simulations and nonlinear characterization of the transition*

Linear stability calculations can predict the critical Reynolds numbers and unstable mode topology and wavelength. However, in order to comprehend the evolution of the instability beyond its onset, nonlinear effects have to be taken into account, and full three-dimensional simulations must be carried out.

The three-dimensional computational calculations utilized the same framework as outlined in § 2.1. However, the spanwise direction was treated using a Fourier expansion in the discretization. This approach was introduced by Karniadakis (1990) and has been often employed since then in cases where the geometry has one homogeneous direction. The meshes utilized in the two-dimensional simulations can

be re-used, since the three-dimensional domains for this type of calculation consist of two-dimensional discretizations repeated in the spanwise direction. In addition, the way the solution algorithm is developed makes the parallelization of the code straightforward and efficient.

The three-dimensional simulation results enabled a nonlinear analysis of the transitions to be conducted. The Landau equation has often been successfully used in hydrodynamics as a low-dimensional model to describe the nonlinear behaviour of transitions close to their respective critical points (see for example Sheard *et al.* 2004; Henderson 1997; Provansal, Mathis & Boyer 1987; Dušek, Le Gal & Fraunié 1994; Noack & Eckelmann 1994). The idea behind this equation is that for a small perturbation amplitude A the linear term determines the behaviour of $\mathrm{d}A/\mathrm{d}t$. If the system is unstable the modulus of A grows and the higher-order terms become important at a certain point. Here, the Landau equation is written up to third order, using the same notation as in Sheard *et al.* (2004):

$$\frac{\mathrm{d}A}{\mathrm{d}t} = (\sigma + \mathrm{i}\omega)\, A - l(1 + \mathrm{i}c)|A|^2 A + \cdots, \tag{2.9}$$

where $A(t)$ is the complex amplitude of the perturbation mode being considered.

The term $(\sigma + \mathrm{i}\omega)$ in (2.9) is the eigenvalue obtained from the linear stability analysis, and in the present case is the Floquet exponent. To first-order approximation, the perturbation grows at a rate given by σ, so the flow is stable if σ is negative and unstable otherwise. In addition, still to first-order approximation, the perturbation oscillates with angular frequency ω, which is non-zero for a Hopf bifurcation. The parameter l is the real part of the third-order coefficient and the classification of the transition depends directly on its sign. If $l > 0$, the transition is supercritical, thus non-hysteretic, and the behaviour of the transition until saturation should be adequately described by the Landau equation truncated at third order. The reason for this is that the real part of the third-order term is negative and counter-balances the growth provoked by the first-order term, eventually making the instability reach a saturated state, so no higher-order terms are necessary. On the other hand, if $l < 0$, the proper description of the transition requires terms of at least fifth order, as both first- and third-order terms promote the growth of A and the numerical and experimental observations indicate that this growth must saturate at some point. In this case, the transition is said to be subcritical. Lastly, c is called the Landau constant and it modifies the oscillation frequency at saturation.

The complex amplitude A can be written in polar form, $A(t) = \rho(t)\mathrm{e}^{\mathrm{i}\Phi(t)}$, and after some simple algebra is performed, the real and imaginary parts of (2.9) become

$$\frac{\mathrm{d}\log(\rho)}{\mathrm{d}t} = \sigma - l\rho^2, \tag{2.10}$$

$$\frac{\mathrm{d}\Phi}{\mathrm{d}t} = \omega - lc\rho^2. \tag{2.11}$$

Given (2.10), a graph of $\mathrm{d}\log(|A|)/\mathrm{d}t$ against $|A|^2$ can be plotted and used to determine the values of σ and l. The value where the curve intercepts the y-axis is σ and the slope of the curve close to the y-axis gives $-l$. If the cubic truncation of the Landau model is sufficient to describe the transition, then this plot should be linear; if not, then at least fifth-order terms are necessary to describe the transition.

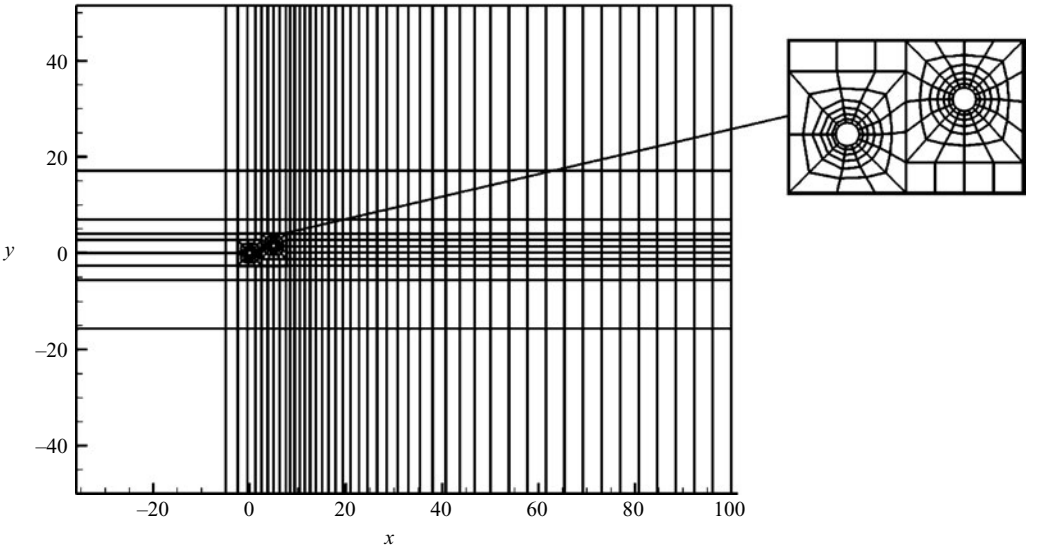

FIGURE 2. Example of a mesh used in the calculations.

Lastly, the amplitude A must be defined in terms of flow variables. In the present work, this amplitude is defined by

$$|A(t)| = \left[\int_{\Omega} |\hat{\boldsymbol{u}}_1(x, y, t)|^2\right]^{1/2},$$

where Ω is the two-dimensional cross-section of the domain being considered and $\hat{\boldsymbol{u}}_1(x, y, t)$ is the coefficient at time t of the Fourier expansion term whose wavenumber is the same as the instability in question. A similar expression was used in Henderson & Barkley (1996) and Henderson (1997); the only difference is a multiplicative constant.

3. Numerical simulations

Figure 1 shows a schematic drawing of the geometry investigated in this research. The two cylinders have the same diameter D. For all cases, the streamwise distance between the centres of the cylinders, L_x, is $5D$. This distance was chosen because, in a previous study that considered pairs of circular cylinders in tandem arrangements with different L_x/D (Carmo 2005), the configuration with $L_x/D = 5$ presented the highest RMS value of the lift coefficient and was outside the L_x/D range for which the transition between different vortex shedding regimes occurs (Mizushima & Suehiro 2005). The transversal distance, L_y, was varied from 0 to $3D$, with intervals of $0.5D$. Calculations were also carried out for the single-cylinder case, which served as a benchmark for comparison with the two-cylinder cases. The Reynolds numbers simulated were 200, 250, 300 and 350, covering the wake transition range for the flow around a single cylinder.

Quadrilateral meshes were generated for the computations; an example is shown in figure 2. The size of the domain and the discretization approach were chosen based on a previous work (Carmo 2005), in which an extensive convergence study was made considering the flow around a single cylinder and using the same numerical method. The upstream boundary (boundary at the left-hand side in figure 2) is located $36D$

from the upstream cylinder centre, the side boundaries (top and bottom boundaries in figure 2) are located $45D$ from the closest cylinder centre and the downstream boundary is located $95D$ from the downstream cylinder. The domains extended far downstream in order to consider the vortex interaction that takes place in the far wake, as reported in § 4.1. The number of elements for the mesh with a single cylinder was 466, and for the meshes with two cylinders the number of elements varied from 568 to 721, depending on L_y. The meshes were the same for all Reynolds numbers, varying only according to the geometrical configuration.

Eighth-degree polynomial expansions were used as basis functions for the spatial discretization, and the integration in time was second-order accurate. The value of the non-dimensional time step varied from 0.004 to 0.006, depending only on the Reynolds number. Uniform stream velocity boundary conditions ($u = 1$, $v = 0$) were imposed at the upstream boundary and upper and lower surfaces of the computational domain. At the cylinder walls, a no-slip condition ($u = 0$, $v = 0$) was imposed, and at the downstream border Neumann boundary conditions, $\partial u/\partial \boldsymbol{n} = 0$, $\partial v/\partial \boldsymbol{n} = 0$ were applied. For the pressure, the high-order boundary condition proposed by Karniadakis *et al.* (1991) was used on all boundaries.

The periodic base flows were calculated using direct numerical simulation, employing the method described in § 2.1. The first step in the process was to let the simulations reach an asymptotic, time-periodic state. In order to check if the system had reached a time-periodic state, the time history of the upstream cylinder lift coefficient calculated at every time step was recorded. Next, ten consecutive peak values and the times at which these peak values occurred in the series were taken. If the ratio between the standard deviation and the mean of these peak values and also the ratio between the standard deviation and the mean of the time interval between two consecutive peaks were less than 0.5%, then the simulation was considered to have reached a periodic state. Subsequently, 32 equally spaced snapshots of the velocity solution were recorded per cycle. These snapshots were used to generate the base flow for the stability calculations. In the single-cylinder cases, only one vortex shedding cycle was considered for the Floquet calculations. However, for all cases with two cylinders, two vortex shedding cycles were used for the Floquet calculations, because the vortex interaction that took place in the far wake had period $2T$, where T is the vortex shedding period (see § 4.1).

For all stability calculations, a Krylov subspace of dimension of 10 was used, and the perturbation initialized with the field $(u', v') = (f, f)$, where f is the positive number that causes the field to have a unitary norm. The calculations were carried out until the residual of the largest eigenvalue reached a value less than 10^{-5}.

The numerical method used here has been previously utilized both for direct numerical simulations (see the examples and references in Karniadakis & Sherwin 2005) and Floquet stability calculations (Barkley & Henderson 1996; Robichaux *et al.* 1999; Sheard *et al.* 2003), in which convergence for these applications has been verified. However, it was necessary to determine whether the size and discretization of the domains were adequate for the cases investigated in the present work.

For this reason, additional simulations were carried out for the cases ($L_y/D = .0$, $Re = 200$), ($L_y/D = 0$, $Re = 350$), ($L_y/D = 3.0$, $Re = 200$), ($L_y/D = 3.0$, $Re = 350$). Two refinements were considered separately: the first was to increase the polynomial degree from 8 to 10, and the second to extend the original mesh by $5D$ on all four external boundaries. For this validation exercise, the base flow was calculated and the Floquet stability analysis was carried out with a fixed value of $\beta D = 2.0$, using the base flow generated with the largest mesh. The parameters monitored in the base flow results

Number of base flow snapshots in two shedding cycles	$L_y/D = 0$		$L_y/D = 3.0$	
	$Re = 200$	$Re = 350$	$Re = 200$	$Re = 350$
16	1.11919	4.66509	0.847345	4.40672
32	1.14009	5.05173	0.860698	4.40394
64	1.13150	4.86170	0.852712	4.20596
128	1.13184	4.85856	0.852498	4.19924

TABLE 1. Convergence of the dominant eigenvalue for $\beta D = 2.0$, varying the number of equally spaced snapshots used to reconstruct the base flow.

were the Strouhal number (St), the mean drag coefficient and the RMS of the lift coefficient, all of which were evaluated for both cylinders, and from the Floquet calculations the value of the Floquet multiplier was also tested for convergence. In all cases, all parameters varied less than 1% when the refined meshes were compared to the reference meshes.

In addition, further tests were performed in order to ensure that considering 32 snapshots per shedding cycle was sufficient to properly reconstruct the base flows. The same cases used in the refinement test were re-run varying the number of base flow snapshots from 16 to 128 over two shedding periods. The results displayed in table 1 show that the difference between the values of the Floquet multiplier obtained using 64 and 128 snapshots over two shedding cycles was less than 0.2%, confirming that 32 snapshots per shedding cycle are enough to satisfactorily describe the base flow.

For the three-dimensional simulations, the meshes and parameters of the corresponding two-dimensional cases were re-used, and periodic boundary conditions were set on the boundary planes located at the extreme values of z.

4. Results

4.1. *Base flow calculations*

The vortex shedding regime in the base flow changed significantly in the range of L_y investigated. The changes in the regime can be observed in figure 3, which shows instantaneous vorticity contours for different L_y. The Strouhal number (St) was calculated by performing a fast Fourier transform of the lift coefficient time history of both cylinders. For every case in the present work, the Strouhal number for the upstream cylinder was the same as obtained for the downstream one.

Analysing figure 3(a), it can be seen that, for $L_y/D = 0$, the vortices shed by the upstream cylinder hit the downstream one. We believe that the pressure and velocity fluctuations imposed near the second body synchronized the vortex shedding. For $0.5 \leqslant L_y/D \leqslant 1.0$, the vortices shed from the upstream cylinder did not directly impinge upon the downstream cylinder, but interacted with the vortex being shed from the lower surface of the downstream cylinder, stretching and pulling it from the near wake of the second cylinder, as shown in figure 3(b). In all cases with $L_y/D \leqslant 1.0$, the vortex interactions that took place in the near wake of the downstream cylinder were notably different from those in the near wake of the upstream cylinder, as we can see in figures 3(a) and 3(b). In the upstream near wake, the interaction between one vortex and the shear layer of opposite-sign vorticity on the other side of the cylinder, which, according to the model proposed in Gerrard (1966), eventually leads to the shedding of a vortex formed in the previous half-cycle, was always very clear.

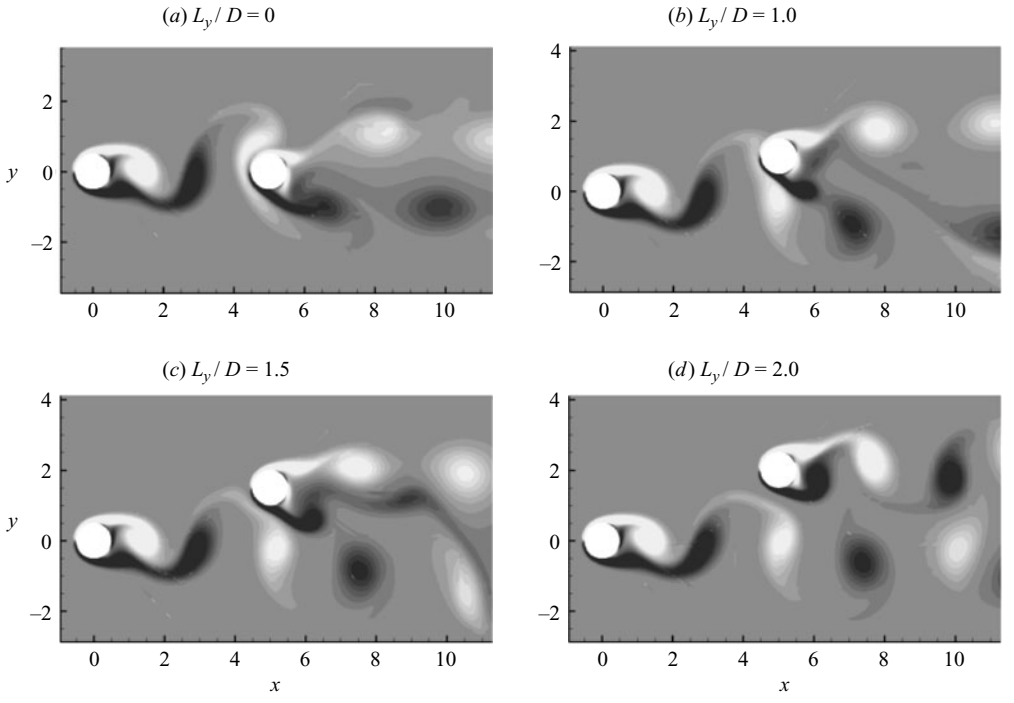

FIGURE 3. Instantaneous vorticity contours, $Re = 200$. Contours vary from $\omega_z D/U_\infty = -2.2$ (light contours) to $\omega_z D/U_\infty = 2.2$ (dark contours).

On the other hand, the shedding in the near wake of the downstream cylinder seemed to be forced by the influence of the upstream wake. The wake of the downstream cylinder was much wider and no strong interactions between vortices and shear layers of opposite sign were observed in the near wake of the downstream cylinder.

We can see in figure 3(*d*) that, for configurations with $L_y/D \geqslant 2.0$, the interaction between vortices of the near wakes of the downstream and upstream cylinders became weaker and the vortices originating from the downstream cylinder were not deformed nor significantly pulled towards the upstream wake. In addition, the shedding mechanisms in both near wakes are very similar, corresponding qualitatively to what happens in the near wake of the flow around a single cylinder. Nevertheless, a synchronization of the wakes due to the proximity of the vortices can still be observed.

The arrangement with $L_y/D = 1.5$ could not be classified into either of the two regimes presented above. The flow around this configuration is in the transition range between these two regimes, being very unstable in terms of the patterns observed in the wake downstream and corresponding to a peak in the absolute value of the mean lift coefficient of the downstream cylinder. In figure 3(*c*), we see that the vortex formed from the bottom of the downstream cylinder (the positive vortex) is split, and part of it merges with the wake of the upstream cylinder, while the rest follows the direction of the downstream cylinder wake. However, this does not occur regularly every cycle; on some occasions the complete vortex is pulled towards the upstream cylinder wake. For $Re \geqslant 250$, the behaviour of the vortex in question in each cycle appears random.

For every configuration with two cylinders, irrespective of the values of L_y and Re, different kinds of vortex interactions were observed in the far wake. This interaction

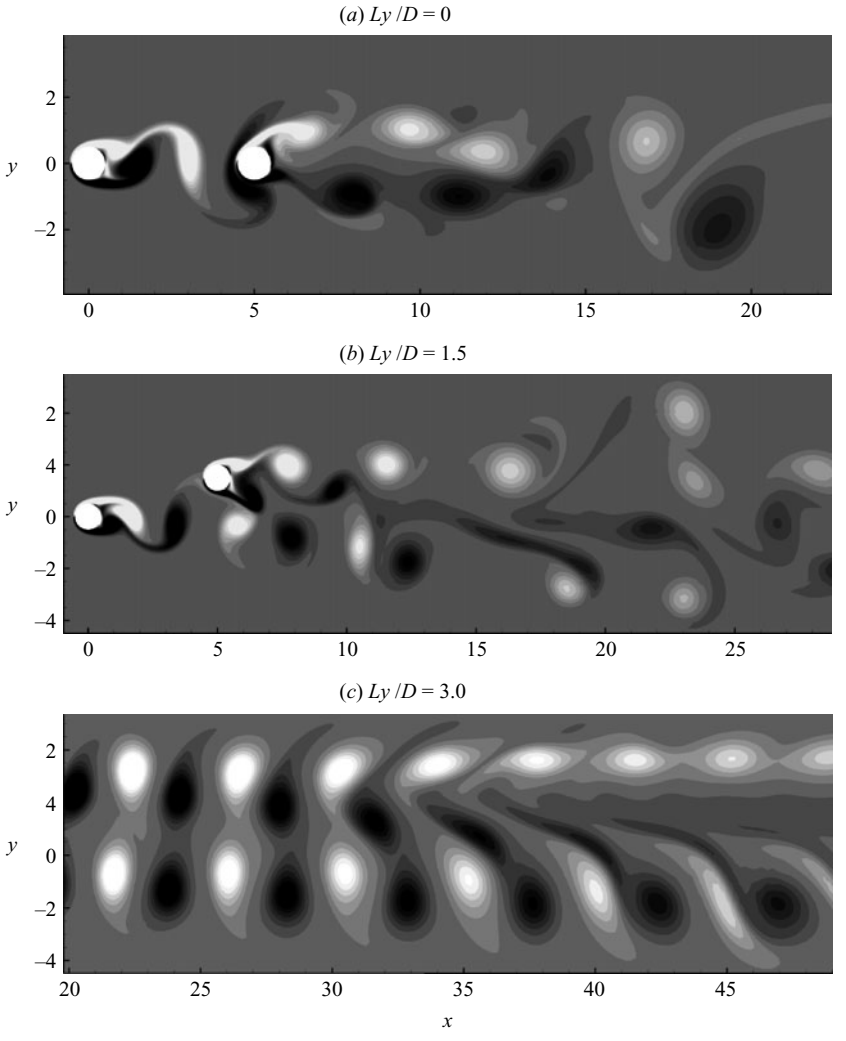

FIGURE 4. Instantaneous vorticity contours, $Re = 250$. Contours vary from $\omega_z D/U_\infty = -2.2$ (light contours) to $\omega_z D/U_\infty = 2.2$ (dark countours) for (a) and (b) and from $\omega_z D/U_\infty = -1.1$ (light contours) to $\omega_z D/U_\infty = 1.1$ (dark countours) for (c).

took place in a limited region, and gave rise to a different vortex configuration in the wake downstream, which will here be referred to as a secondary wake. The secondary wake had a period of $2T$, where T was the period of vortex shedding, because its formation always involved the merging of vortices from two successive cycles. Figure 4 shows instantaneous vorticity contours, focusing on the vortex interaction region that arises in the far wake, for three different configurations. It should be noted that the type of interaction is very different in each of the illustrated cases, although all of them involve vortex merging. For $L_y/D \leqslant 1.5$, this vortex interaction region appears between $10D$ and $20D$ downstream of the front cylinder, while for configurations of higher L_y, when two distinct wakes are observed, this region appears further downstream, at distances as far as $30D$ downstream of the front cylinder. Similar patterns in the far wake were observed in smoke visualizations performed by Zdravkovich (1972) for different tandem and staggered arrangements.

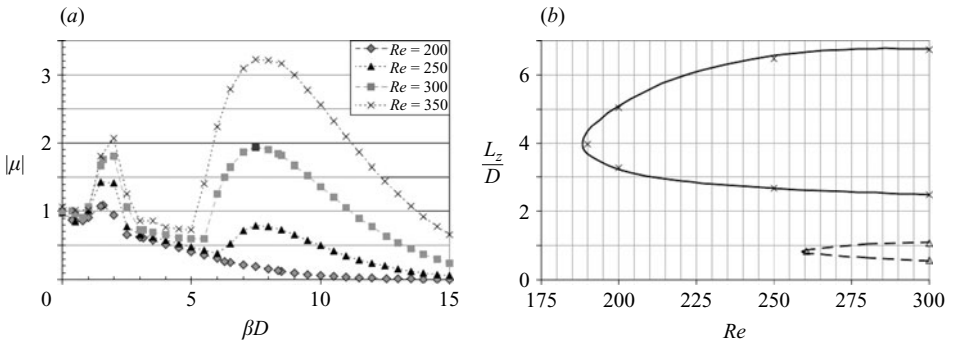

FIGURE 5. Flow around a single cylinder. (*a*) Modulus of the Floquet multiplier, $|\mu|$, as a function of the spanwise wavenumber times the cylinder diameter, βD, for various Reynolds numbers. (*b*) Neutral stability curves (curves that pass through points where $|\mu| = 1$), plotted in a map of Reynolds number (x-axis) and mode non-dimensional wavelength (y-axis); in the region on the right hand side of the curves the two-dimensional periodic flow is unstable with respect to three-dimensional perturbations; continuous and dashed curves are from Barkley & Henderson (1996) and refer to modes A and B respectively; ×, mode A neutral points, present investigation; Δ, mode B neutral points, present investigation.

4.2. *Floquet stability calculations*

4.2.1. *Single cylinder*

In order to validate the code and to have a benchmark for the other cases, the first stage of the stability calculations consisted of the Floquet analysis of the flow around a single cylinder. For this particular configuration, we used 32 equispaced time slices taken from a single vortex shedding period T to use in a temporal Fourier representation of the base flow. The values of the modulus of the Floquet multiplier, $|\mu|$, for these calculations are shown in figure 5(*a*). Two different unstable modes are present in the considered Reynolds number range. Following the nomenclature suggested by Williamson (1988), they are called modes A and B. Mode A, which corresponds to the peaks of lowest βD in each of the curves shown in figure 5(*a*), is, in terms of Reynolds number, the first to appear, and is already unstable at $Re = 200$. For this mode, the wavelength of maximum growth rate is around $4.0D$. Mode B corresponds to the peak of higher βD, having a wavelength of maximum growth rate of about $0.8D$, and, among the cases calculated, it is only unstable for $Re = 300$ and $Re = 350$, although a peak can already be seen in the stable region for $Re = 250$. Figure 5(*b*) shows the good agreement between the neutral stability curves for modes A and B presented by Barkley & Henderson (1996) and some points of neutral stability calculated in the present work. The critical Reynolds numbers and corresponding perturbation wavelengths in the present study were $Re_A = 190 \pm 1$, $L_{zA}/D = 3.97 \pm 0.01$ for mode A and $Re_B = 260.5 \pm 1.0$, $L_{zB}/D = 0.825 \pm 0.010$ for mode B. These values coincide with those reported in Barkley & Henderson (1996) ($Re_A = 188.5 \pm 1.0$, $L_{zA}/D = 3.96 \pm 0.02$ and $Re_B = 259 \pm 2$, $L_{zB}/D = 0.822 \pm 0.007$) within the uncertainty bounds.

An important difference between modes A and B is their spatio-temporal symmetry (Barkley & Henderson 1996; Blackburn *et al.* 2005). The three-dimensional structure of the normalized Floquet mode associated with a spanwise wavenumber β can be reconstructed by considering the perturbation in the vector form:

$$\boldsymbol{u}'(x, y, z, t) = [\tilde{u}(x, y, t)\cos\beta z]\hat{\boldsymbol{i}} + [\tilde{v}(x, y, t)\cos\beta z]\hat{\boldsymbol{j}} + [\tilde{w}(x, y, t)\sin\beta z]\hat{\boldsymbol{k}}. \quad (4.1)$$

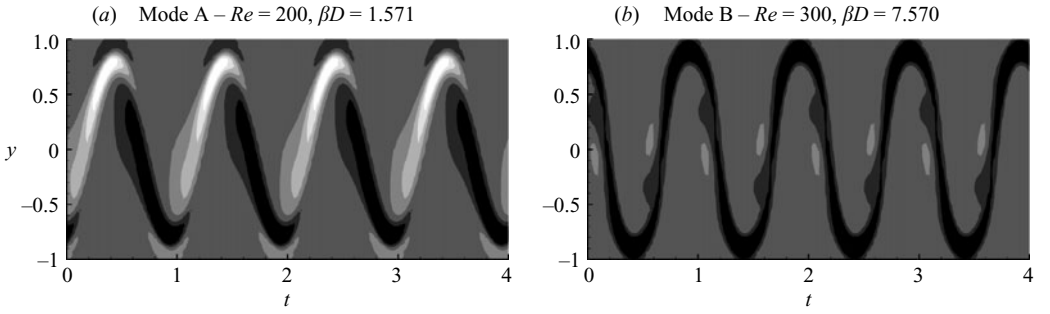

FIGURE 6. x-vorticity of the unstable eigenvector on the line $x = 2.0D$. Light regions correspond to negative and dark to positive streamwise vorticity of the eigenvector. Time is non-dimensionalized using the shedding period.

The perturbation vorticity field can be calculated using the modified nabla operator $\nabla_\beta = (\partial/\partial x, \partial/\partial y, -\mathrm{i}\beta)$, leading to

$$\omega(x, y, z, t) = [\tilde{\omega}_x(x, y, t)\sin\beta z]\hat{\boldsymbol{i}} + [\tilde{\omega}_y(x, y, t)\sin\beta z]\hat{\mathrm{j}} + [\tilde{\omega}_z(x, y, t)\cos\beta z]\hat{\boldsymbol{k}}. \quad (4.2)$$

The T-periodic base flow obeys a reflectional symmetry about the wake centreline ($y = 0$), when time is advanced by $T/2$. Following Robichaux *et al.* (1999), this symmetry is called RT symmetry (R for reflectional and T for translation in time). Mode A has the following RT symmetry:

$$\text{Mode A} : \begin{cases} \tilde{u}(x, y, z, t) = \tilde{u}(x, -y, z, t + T/2), \\ \tilde{v}(x, y, z, t) = -\tilde{v}(x, -y, z, t + T/2), \\ \tilde{w}(x, y, z, t) = \tilde{w}(x, -y, z, t + T/2), \end{cases} \quad (4.3)$$

which is the same as the symmetry of the two-dimensional base flow. In contrast, mode B has the opposite symmetry to mode A:

$$\text{Mode B} : \begin{cases} \tilde{u}(x, y, z, t) = -\tilde{u}(x, -y, z, t + T/2), \\ \tilde{v}(x, y, z, t) = \tilde{v}(x, -y, z, t + T/2), \\ \tilde{w}(x, y, z, t) = -\tilde{w}(x, -y, z, t + T/2). \end{cases} \quad (4.4)$$

Most of the published results regarding these modes focus on the streamwise vorticity component. Using (4.3), the following expression for the x-component vorticity ω_x on mode A is derived:

$$\tilde{\omega}_x(x, y, z, t) = -\tilde{\omega}_x(x, -y, z, t + T/2). \quad (4.5)$$

For mode B, using (4.4), the streamwise vorticity is found to obey the symmetry

$$\tilde{\omega}_x(x, y, z, t) = \tilde{\omega}_x(x, -y, z, t + T/2). \quad (4.6)$$

In figure 6, streamwise vorticity contours evaluated in time on a vertical line $2D$ downstream of the cylinder are presented. The symmetry of the form and absolute strength of the vortices can be clearly observed. For mode A, the vorticity has different sign each side of the wake centreline; for mode B, the vorticity has the same sign throughout the cycle.

4.2.2. *Staggered arrangements*

Having reviewed the single-cylinder case, we now consider the stability of the periodic flow around pairs of cylinders in staggered arrangements. For these cases, two shedding periods were considered, taking into account the $2T$-periodicity of

L_y/D	Re_A	L_{zA}/D	Re_B	L_{zB}/D	Re_C	L_{zC}/D
0.0	**180**	**3.78**	272	0.82	–	–
0.5	**180**	**3.79**	275	0.82	–	–
1.0	**183**	**3.86**	–	–	191	1.55
2.0	190	3.94	265	0.83	**178**	**1.65**
2.5	**192**	**3.97**	264	0.83	198	1.45
3.0	**193**	**3.98**	263	0.83	209	1.45
Single cylinder	**190**	**3.97**	260.5	0.825	–	–

TABLE 2. Critical Reynolds numbers and corresponding perturbation wavelengths. The critical Reynolds numbers have an uncertainty of ± 1 and the corresponding perturbation non-dimensional wavelengths have an uncertainty of ± 0.01 for all cases. The pair $(Re, L_z/D)$ for which the wake first becomes three-dimensional in each configuration is written in bold face.

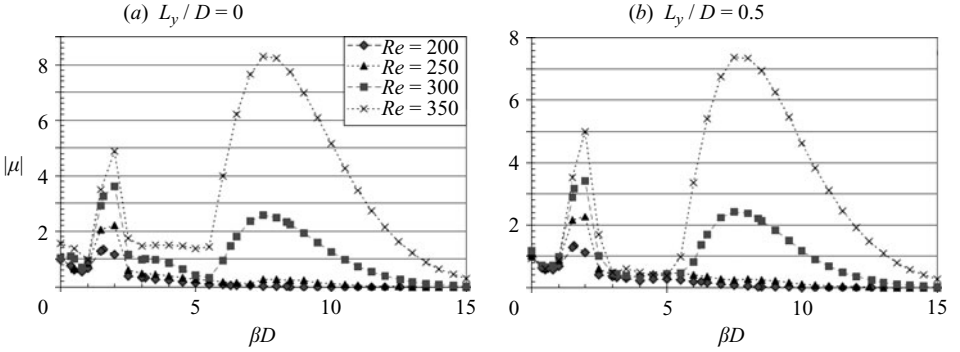

FIGURE 7. Modulus of the Floquet multiplier, $|\mu|$, as a function of the spanwise wavenumber times the cylinder diameter, βD, for various Reynolds numbers.

the far wake. Thus, 64 time slices of the two-dimensional simulations were used to generate each periodic base flow. Owing to its transitional character, the case with $L_y/D = 1.5$ did not present a reasonably periodic wake for any of the Reynolds numbers tested. Therefore no Floquet stability results are presented for this case, since the level of uncertainty of the calculations would be too high for a proper analysis.

For small L_y (more specifically for $L_y/D = 0$ and 0.5) the shape of the curves $|\mu|$ versus βD was similar to the single-cylinder case. Figure 7 shows the values of $|\mu|$ for the configurations with $L_y/D = 0$ and 0.5. The two peaks, corresponding to mode A and mode B, are clearly evident. There are significant changes, however. Table 2 shows that for $L_y/D = 0$ and 0.5 mode A becomes unstable earlier in terms of Reynolds numbers compared to the single-cylinder case, and the wavelength of the unstable mode at the bifurcation is somewhat shorter. Moreover, the growth per shedding period computed for $L_y/D = 0$ and 0.5 in the range corresponding to mode A was larger than those for the single cylinder at the same Reynolds number and spanwise wavenumber (the growth per shedding period is equal to the square root of the values plotted in figure 7 for $L_y/D = 0$ and 0.5 and equal to the values plotted in figure 5(*a*) for the single cylinder). On the other hand, mode B becomes unstable later, in terms of Reynolds number, for $L_y/D = 0$ and 0.5 than for the single-cylinder case, and the wavelength of the unstable mode at the bifurcation is approximately

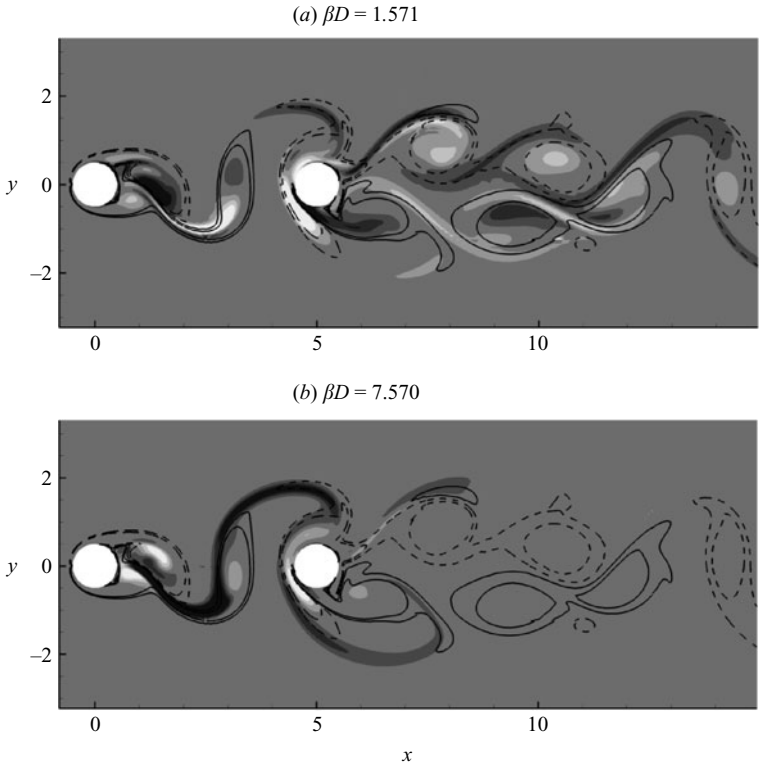

FIGURE 8. Instantaneous streamwise vorticity contours of eigenvectors (greyscale) superposed on spanwise vorticity contours of the base flow (lines), for flow around two cylinders with $L_y/D = 0$, $Re = 300$. Light regions correspond to negative and dark to positive x-vorticity of the eigenvector. The solid and dashed lines represent positive and negative z-vorticity contours of the base flow respectively.

the same. Also in contrast with the behaviour observed for mode A, the growth per shedding period in the range corresponding to mode B was smaller for $L_y/D = 0$ and 0.5 than for the single cylinder.

In order to examine the structure of the modes for $L_y/D = 0$ and 0.5 in greater detail, figure 8 shows streamwise vorticity contours of the unstable eigenvectors. Figure 8(a) shows structures characteristic of mode A. Of note is that the instability first develops in the near wake of the upstream cylinder, but then grows stronger when it reaches the downstream cylinder. Also of note is the strong streamwise vorticity in the region of vortex interaction that initiates the secondary wake. It seems that the vortex merging and straining that occur in this region helps to reinforce mode A structures. The results are different for mode B. In figure 8(b), we see that the instability first develops in the near wake of the upstream cylinder, as in the mode A case. However, the streamwise vortical structures do not seem to gain significant strength when they impinge upon the downstream cylinder. Also, no mode B structures were observed in the vortex interaction region that initiates the secondary wake.

For $L_y/D = 1.0$, the transition deviates from that observed for the flow around a single cylinder. A peak of intermediate wavenumber dominates, as can be seen in figure 9(a). This corresponds to mode C, which will be described and analysed in more detail in § 4.3. The peak relating to mode B is only visible for $Re = 350$;

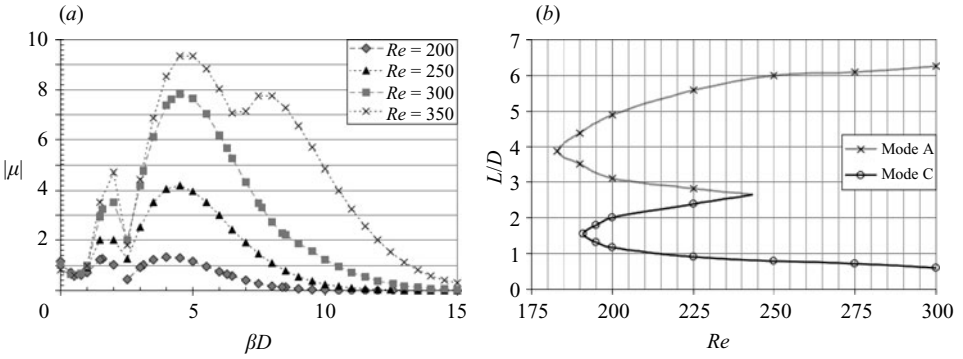

FIGURE 9. Flow around a pair of cylinders with $L_y/D = 1.0$. (*a*) Modulus of the Floquet multiplier, $|\mu|$, as a function of the spanwise wavenumber times the cylinder diameter, βD, for various Reynolds numbers. (*b*) Neutral stability curves.

nevertheless it was verified that this mode is already unstable for $Re = 300$, but that the corresponding Floquet multiplier is smaller than that relating to mode C. Figure 9(*b*) shows the neutral stability curves for this configuration, and the critical Reynolds numbers and corresponding perturbation wavelengths are displayed in table 2. The critical Reynolds number for which mode A became unstable was considerably lower than for a single cylinder, and the corresponding wavelength was somewhat smaller.

For configurations in which two distinct wakes could be observed ($2.0 \leqslant L_y/D \leqslant 3.0$), mode C was also detected. The graphs on the left-hand side of figure 10 exhibit three distinct peaks, and the peak relating to mode C appears in a region of intermediate wavenumbers, between the peaks associated with modes A and B.

The right hand side of figure 10 shows the neutral stability curves for the same configurations, and the critical Reynolds numbers and corresponding perturbation wavelengths are also displayed in table 2. For the three cases, mode A and mode B critical Reynolds numbers and corresponding perturbation wavelengths were close to the values found for the isolated-cylinder case. Nevertheless, the neutral stability curve for mode C differed considerably when these cases are compared. Table 2 shows that mode C becomes unstable later at a progressively increasing Re as L_y increases; the right-hand side of figure 10 shows that the region of mode C instability becomes thinner. This behaviour is not surprising, given that the larger the distance between the cylinders, the closer the flow is to the single-cylinder case, for which no mode C instability is observed.

Another result worth mentioning is that, for $2.0 \leqslant L_y/D \leqslant 3.0$, $Re = 300$ and 350, convergence of the second-most leading Floquet multiplier was also possible for a few wavenumbers in the ranges associated with modes A and B. Indeed, the Floquet modes associated with these multipliers did correspond to the appearance of modes A and B in the near wake of the downstream cylinder. However, a systematic analysis of these modes was not possible since we were unable to satisfactorily converge the second leading Floquet multiplier for all wavenumbers.

4.3. *Mode C*

In this section, the intermediate-wavenumber mode that appeared in the wake transition for $L_y/D = 1.0$, 2.0, 2.5 and 3.0 is examined. This mode is in fact a mode C instability (Zhang *et al.* 1995; Sheard *et al.* 2003), as will be shown later,

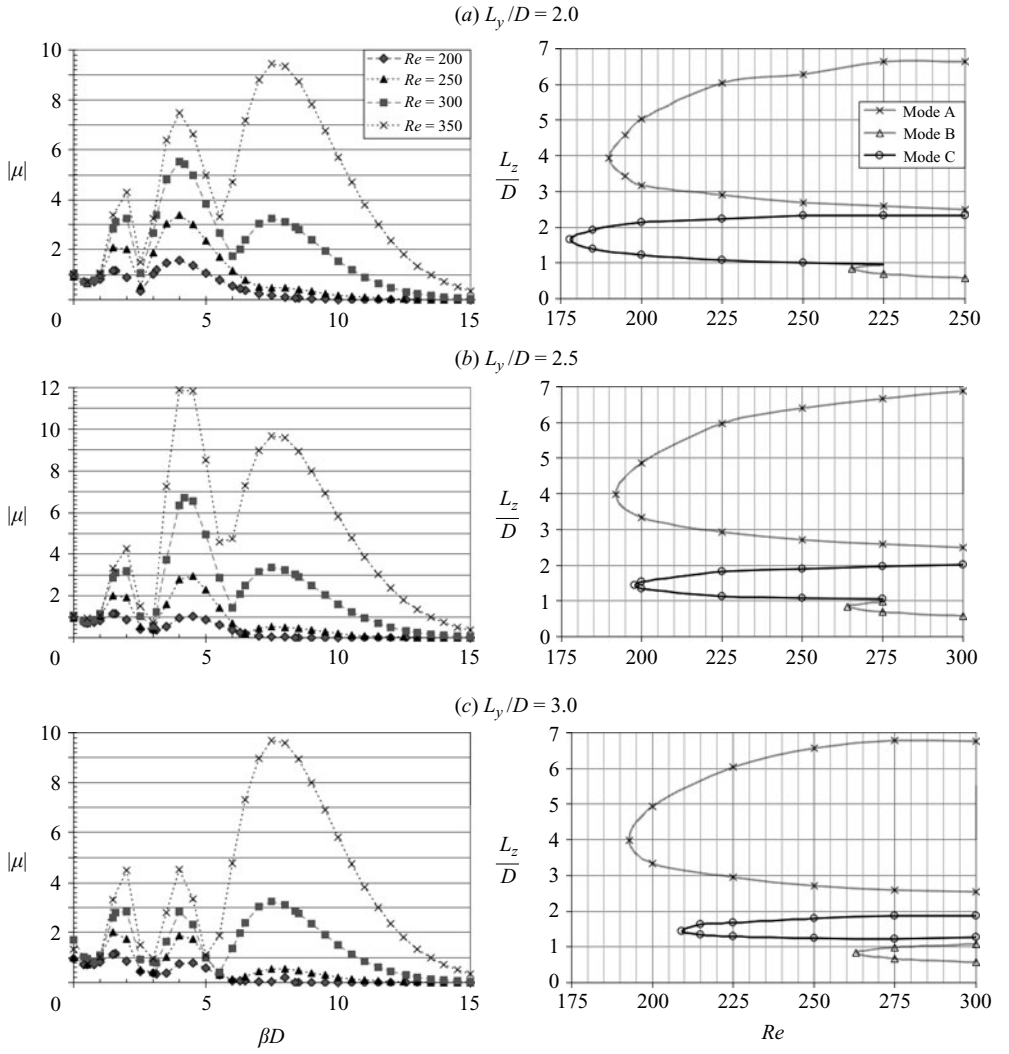

FIGURE 10. Modulus of the Floquet multiplier, $|\mu|$, as a function of the spanwise wavenumber times the cylinder diameter, βD, for various Reynolds numbers (left-hand side) and neutral stability curves (right-hand side). Flow around staggered arrangements.

so this designation will be used from now on. Figure 11 shows instantaneous x-vorticity contours of an eigenvector of mode C. A significant difference between this mode and modes A and B is that mode C originates in the near wake of the downstream cylinder, while modes A and B first appear in the near wake of the upstream cylinder. The region where mode C develops has a dominant frequency equal to the shedding frequency, unlike the far-wake region, which has a dominant frequency of half the shedding frequency. The Floquet multiplier for mode C using a two-dimensional base flow comprising two shedding cycles was real and positive. In order to verify if the mode in question was a synchronous or a period-doubling mode, additional calculations were carried out, considering only one shedding period of the two-dimensional base flow in the Floquet analysis, which corresponds to a single Poincaré map. The results lead to real negative Floquet multipliers, therefore

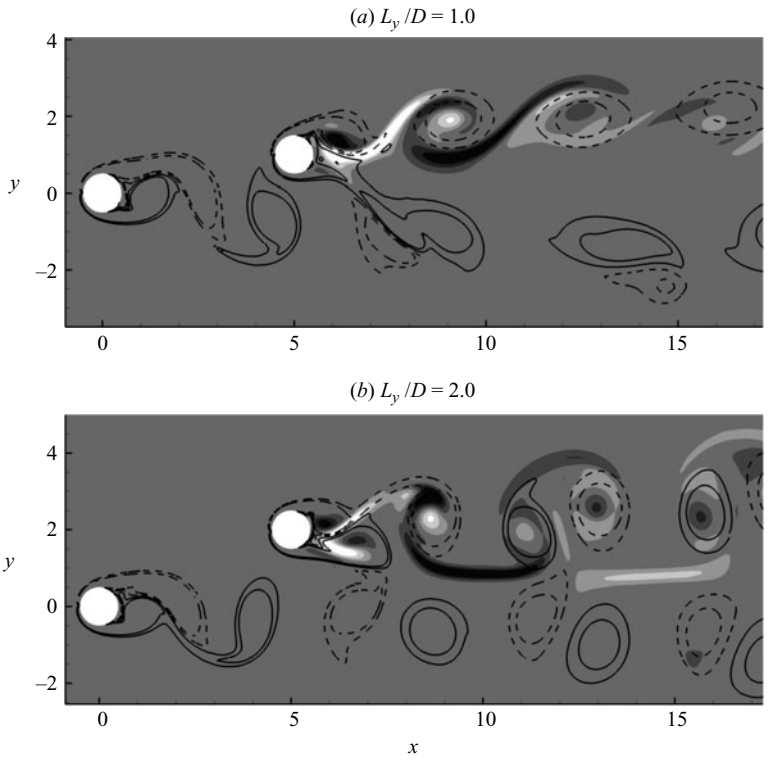

FIGURE 11. Instantaneous streamwise vorticity contours of the eigenvector (greyscale) superposed on spanwise vorticity contours of the base flow (lines), $Re = 200$, $\beta D = 4.0$. Light regions correspond to negative and dark to positive streamwise vorticity of the eigenvector. The solid and dashed lines represent positive and negative z-vorticity contours of the base flow respectively.

demonstrating that the mode is a three-dimensional period-doubling instability on the two-dimensional base flow of one shedding period, just like the mode C instability reported by Sheard *et al.* (2003).

Comparing figures 11(*a*) and 11(*b*), it is possible to see that the streamwise vorticity contours of mode C have striking differences in shape depending on the shedding mode. For $L_y/D = 1.0$, the positive vortices shed from the downstream cylinder in the base flow are pulled away from the body by the vortices that are shed from the upstream cylinder. Consequently, the negative vortices form an isolated vortex line, where mode C develops. This is an extreme case of wake asymmetry. For $L_y/D \geqslant 2.0$ (figure 11*b*), a complete wake is being formed after the downstream cylinder, so the level of asymmetry is much weaker, although doubtless present. In such cases mode C streamwise vorticity can be observed in both sides of the wake.

Figure 12 shows the time history of the x-vorticity contours of the eigenvector of mode C on a vertical line $2D$ aft of the downstream cylinder ($7D$ aft the upstream cylinder). The first important aspect to notice is that this mode is not symmetric in relation to the wake centreline (in figure 12, the wake centreline is $y = 2D$). A second aspect of note is that this mode has a period of $2T$, where T is the shedding period, in contrast with modes A and B, which are T-periodic. The symmetry of mode C is

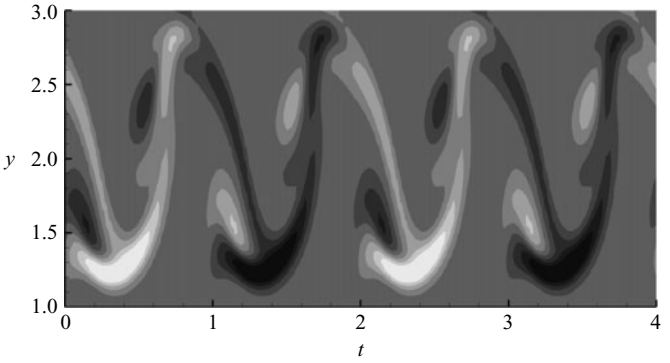

FIGURE 12. Normalized x-vorticity of the unstable eigenvector on the line $x = 7D$, configuration $L_y/D = 2.0$, $Re = 300$ and $\beta D = 4.0$. Light regions correspond to negative and dark to positive streamwise vorticity of the eigenvector. Time is non-dimensionalized using the shedding period.

thus only temporal, and has the form

$$\text{Mode C:} \begin{cases} \tilde{u}(x, y, z, t) = -\tilde{u}(x, y, z, t + T), \\ \tilde{v}(x, y, z, t) = -\tilde{v}(x, y, z, t + T), \\ \tilde{w}(x, y, z, t) = -\tilde{w}(x, y, z, t + T), \end{cases}$$

which translates to the streamwise vorticity:

$$\tilde{\omega}_x(x, y, z, t) = -\tilde{\omega}_x(x, y, z, t + T).$$

Figure 13 shows plots of vorticity iso-surfaces of the base flow combined with the unstable Floquet mode for modes A, B and C. The three-dimensional structures of modes A and B are very similar to those observed in the flow around a single cylinder (Henderson 1997). For mode A, the streamwise vorticity is stronger in the primary vortex cores, whereas for mode B it is stronger in the braid shear layers. This similarity in the structures is not surprising given the already mentioned similarities in the symmetry and wavelength. Apart from the different wavelength and its period-doubling nature, mode C presents a structure similar to mode B, in the sense that it is stronger in the braid shear layers. The asymmetrical nature of mode C is also clear in the figure, as the stronger streamwise vorticity is observed in the side of the wake closest to the vortex street formed from the upstream cylinder.

Figure 14 shows two snapshots of spanwise vorticity iso-surfaces of the unstable mode C added to the base flow, taken at time instants one flow period apart. The period-doubling character of mode C makes the waviness of the vortex cores at the same location at consecutive periods have a phase difference of 180°, as can be observed looking to the far left vortices in figure 14. Another evidence of the period-doubling character displayed in figure 14 is the alternation of the sign of the spanwise vorticity, from one period to the next, in the shear layers close to the cylinder.

As previously mentioned, the period-doubling mode C was also identified by Sheard *et al.* (2003), in stability calculations of the flow around bluff rings with aspect ratio (ratio between the ring diameter and the cross-section diameter) greater than 4.0. In that work they found a maximum growth rate for mode C for spanwise wavelengths between $1.6D$ and $1.7D$, which agrees well with the results of the present investigation. They also reported that the smaller the aspect ratio was, the earlier

(*a*) Mode A, $L_z/D = 4.000$

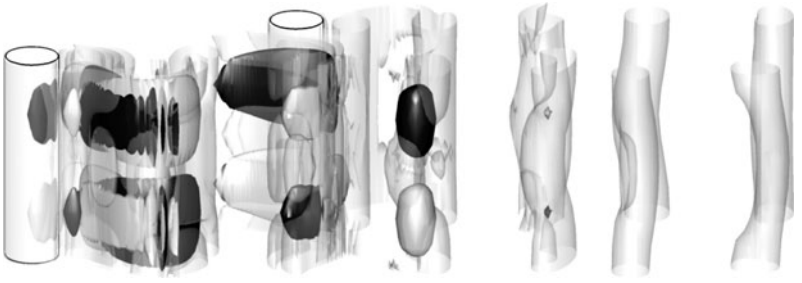

(*b*) Mode B, $L_z/D = 0.830$

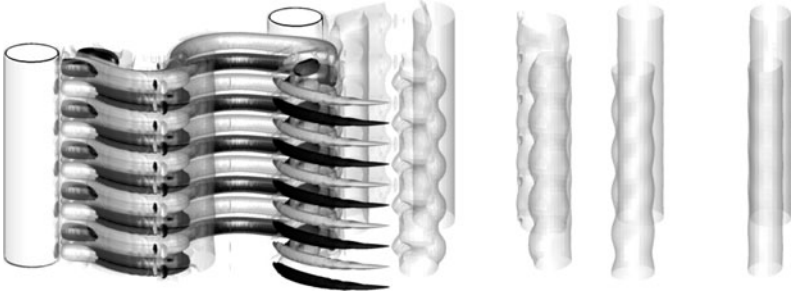

(*c*) Mode C, $L_z/D = 1.570$

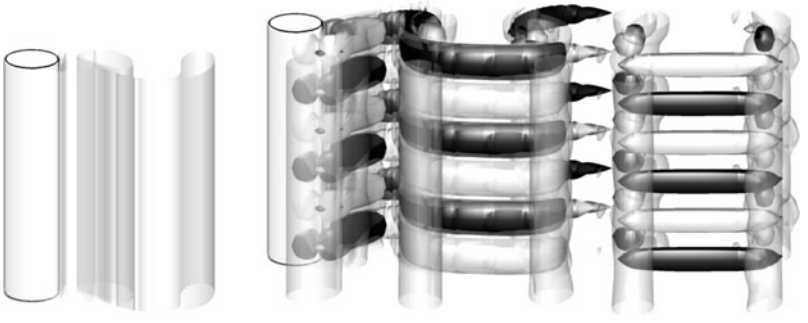

FIGURE 13. Three-dimensional structures of the unstable modes, configuration $L_y/D = 2.0$, $Re = 300$. The represented flow fields are linear combinations of the base flow and the unstable Floquet mode. Translucent surfaces are iso-surfaces of $|\omega_z|$. Solid light grey and dark grey surfaces are iso-surfaces of negative and positive ω_x respectively.

(in terms of Reynolds number) mode C became unstable. The same behaviour was observed in our staggered cylinder arrangements when $L_y/D \geqslant 2.0$, if we replace the aspect ratio by L_y/D, as discussed in § 4.2.2. Furthermore, striking similarities between the three-dimensional structure of mode C are found when comparing figure 13 to the results presented in Sheard *et al.* (2004). The mode C wavelength found in the present results is also reasonably close to the value of $1.8D$ reported in Zhang *et al.* (1995). In that study, mode C appeared in their experiments when a thin control wire was placed near the cylinder, and they reproduced this result in computational simulations by enforcing zero velocity at the point of the mesh that corresponded to

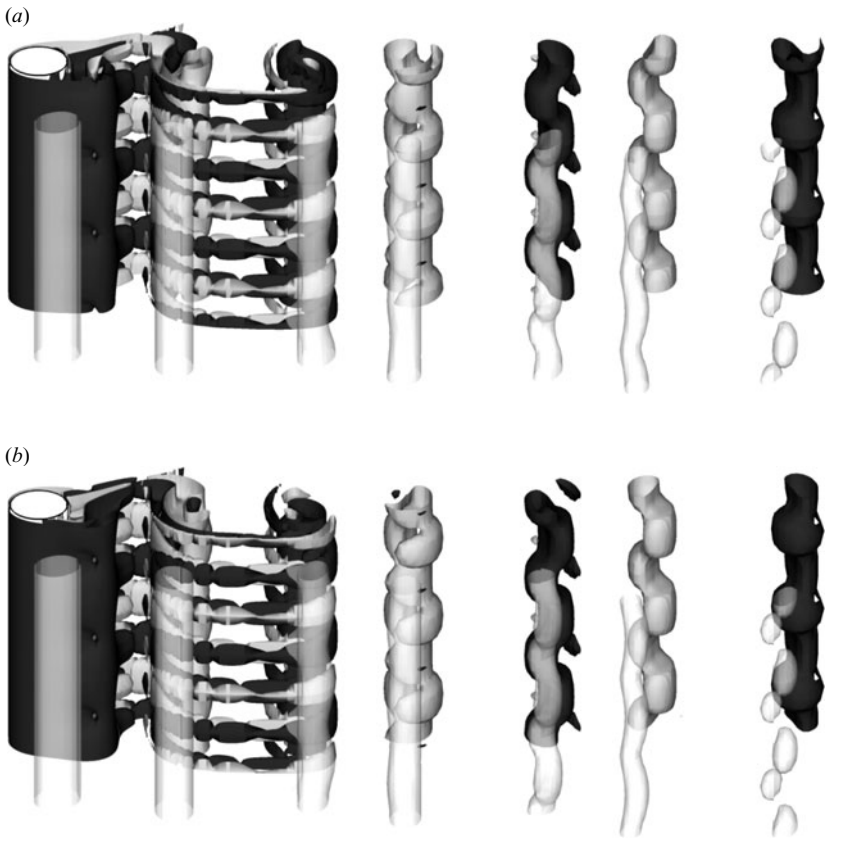

FIGURE 14. Iso-surfaces of spanwise vorticity, unstable mode added to base flow, configuration $L_y/D = 2.0$, $Re = 300$, $L_z/D = 1.570$. The cylinder shown is the downstream cylinder. Solid iso-surfaces are vorticity shed by the downstream cylinder (light grey iso-surfaces are negative ω_z and dark grey are positive ω_z), and translucent iso-surfaces are vorticity shed by the upstream cylinder (iso-surfaces of same absolute value of ω_z as in the solid iso-surfaces). (*a*) Snapshots at time (*a*) t and (*b*) $t + T$.

the coordinate of the centre of the control wire. We note that asymmetry is again involved in the base flow.

4.4. *Nonlinear analysis*

In order to investigate the nonlinear evolution of mode C, fully three-dimensional simulations were also performed. The configurations $L_y/D = 1.0$, 2.0, 2.5 and 3.0 were tested, and Reynolds numbers slightly higher than the critical Reynolds number for mode C bifurcation (Re_c) for each configuration were selected. For each case, the periodic span of the domain was the wavelength of the mode C instability at its onset and the initial condition was the unstable Floquet mode, multiplied by a factor small enough to make the initial growth linear, added to the two-dimensional periodic solution at a fixed time. This method of choosing the periodic length and the initial condition was also adopted in Henderson & Barkley (1996) and Henderson (1997), and has the advantage of enabling the clear observation of the evolution of the mode. In all calculations reported in this subsection, eight Fourier modes were used in the discretization in the spanwise direction.

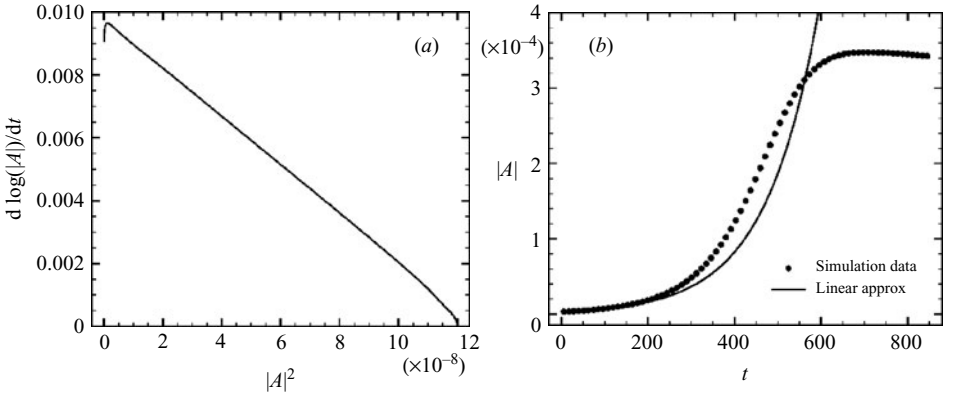

FIGURE 15. Results for three-dimensional simulation of case $L_y/D = 1.0$, $Re = 195$, $L_z/D = 1.55$. (*a*) The derivative of the amplitude logarithm against the square of the amplitude. (*b*) The growth and saturation of the amplitude in the wavelength corresponding to the mode C instability (symbols) and growth predicted by linear calculations (continuous line). The x-axis is non-dimensional time.

4.4.1. $L_y/D = 1.0$

In figure 15(*a*), it can be seen that the curve of the derivative of the amplitude logarithm against the square of the amplitude has a positive slope close to the y-axis, hence the bifurcation for mode C was subcritical for the configuration with $L_y/D = 1.0$. It is worth noting how small is the range of $|A|^2$ for which the curve has a positive slope when compared to other cases of subcritical bifurcation (see, for example, figure 17(*a*) of this paper and the cases of subcritical bifurcation in Sheard *et al.* 2004). After this range, the curve follows an approximately straight line of negative slope. In order to check if this region of positive slope was due only to a initial transient and therefore not truly an indication of subcritical behaviour, a decay test was performed, in which the saturated three-dimensional flow at $Re = 195$, which is above Re_C, was used as initial condition for a simulation with $Re = 187$, which is below Re_C. By performing this test, we can ensure that the behaviour close to $|A|^2 = 0$ is free from any initial transient effects. The result showed a positive slope in the vicinity of $|A|^2 = 0$, confirming that the bifurcation is indeed subcritical. Further evidence of the subcritical character can be found in figure 15(*b*), which shows that, before saturation, the actual growth of the mode energy is clearly higher than the prediction given by the linear calculations.

4.4.2. $L_y/D = 2.0$ *and* 2.5

The mode C bifurcation in these two configurations presented a supercritical character, as can be seen in the graphs plotted in figures 16(*a*) and 16(*c*), which have negative slopes for their entire range. The curves in these figures are linear until fairly close to saturation; therefore, the nonlinear evolution of the mode within this linear range can be described by a Landau equation with terms up to third order. The coefficients of the Landau equation were calculated for both cases, and in figures 16(*b*) and 16(*d*) it can be seen that the results of the simulations agree very well with the Landau predictions until close to saturation. Since the difference between the two curves is very small, we believe that the introduction of the fifth-order term in the equation should be enough to provide a proper description of the instability evolution. The third-order Landau equations predict a higher value of the saturated

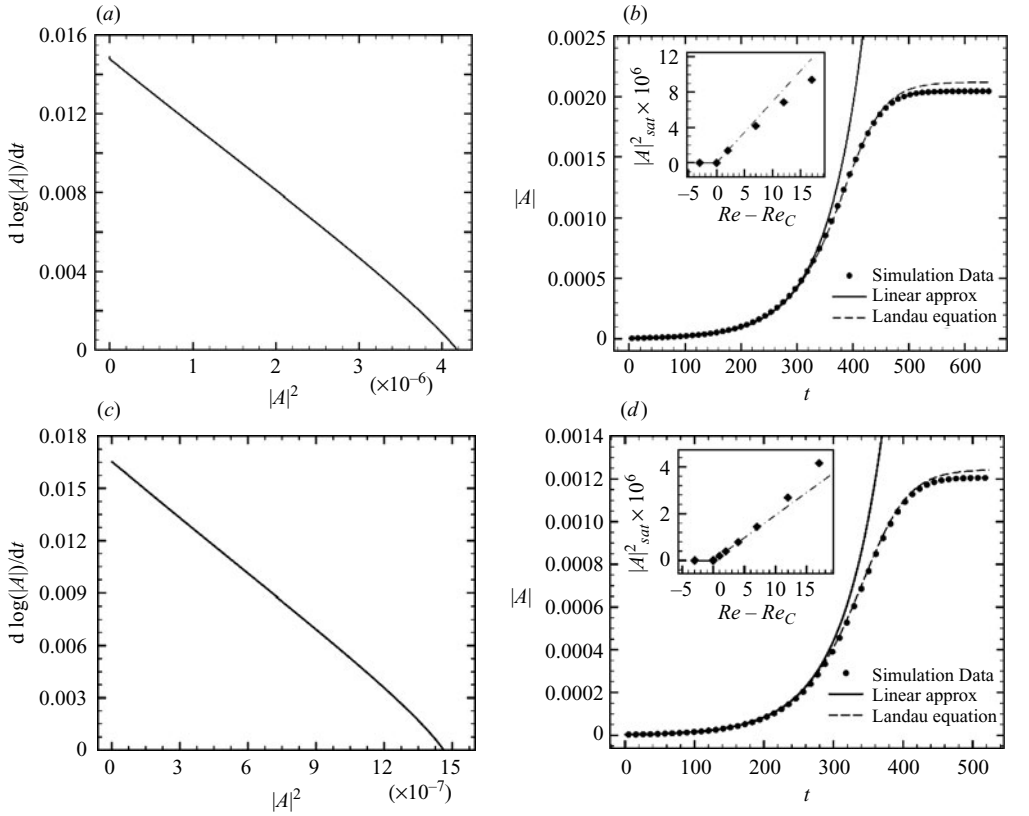

FIGURE 16. Results for three-dimensional simulation of cases $L_y/D = 2.0$, $Re = 185$, $L_z/D = 1.65$ (a, b) and $L_y/D = 2.5$, $Re = 205$, $L_z/D = 1.45$ (c, d). (a, c) The derivative of the amplitude logarithm against the square of the amplitude. (b, d) The growth and saturation of the amplitude in the wavelength corresponding to the mode C instability (symbols), growth predicted by linear calculations (continuous line) and growth predicted by the Landau equation (dashed line). The x-axis is non-dimensional time. The insets of these figures show diagrams of the supercritical bifurcations.

amplitude than the results given by the simulations, both for $L_y/D = 2.0$ and 2.5; therefore we conclude that the coefficient of the fifth-order term should be negative.

The insets on figures 16(b) and 16(d) show that the energy approaches zero gradually when the Reynolds number is decreased towards the critical value. Diagrams with this shape are typical of supercritical bifurcations.

4.4.3. $L_y/D = 3.0$

For this particular configuration, the mode C bifurcation showed a subcritical character, as can be inferred from the curve in figure 17(a), which exhibits a positive slope close to the y-axis and whose non-rectilinear shape indicates that terms of order higher than three must be considered in the Landau equation to adequately describe the nonlinear evolution of the instability. Another subcritical attribute of the bifurcation can also be discerned by analysing figure 17(b), where the energy related to mode C wavelength, obtained from the three-dimensional simulations, grows at a higher rate than that predicted by the linear theory. The inset in this figure shows the hysteresis present in the vicinity of the critical point.

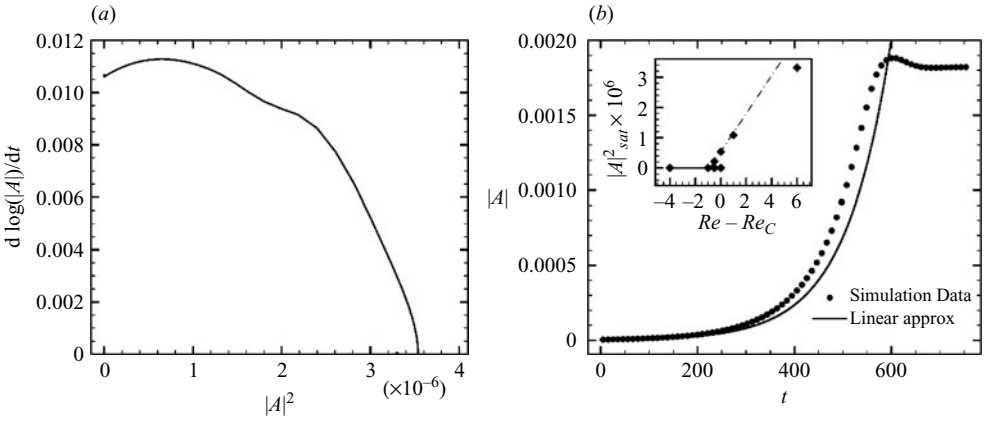

FIGURE 17. Results for three-dimensional simulation of case $L_y/D = 3.0$, $Re = 215$, $L_z/D = 1.45$. (*a*) The derivative of the amplitude logarithm against the square of the amplitude. (*b*) The growth and saturation of the amplitude in the wavelength corresponding to the mode C instability (symbols) and growth predicted by linear calculations (continuous line). The x-axis is non-dimensional time. The inset of (*b*) show a diagram of the subcritical bifurcation.

In order to check if the period-doubling mode C leads to a period-doubling cascade after the secondary instability, some additional three-dimensional simulations were performed using a periodic spanwise wavelength of $12.0D$. Runs with $Re = 350$ were carried out for all configurations. Extra simulations were also performed for ($L_y/D = 1.0$, $Re = 200$), ($L_y/D = 2.0$, $Re = 200$) and ($L_y/D = 3.0$, $Re = 250$), since for these intermediate cases only modes A and C were unstable and we were interested to know how these modes interacted in the absence of mode B.

Velocity time histories at diverse points in the wake were monitored, and for all configurations, no sign of a period-doubling cascade was observed. The spectra of the velocity in the x- and y-directions were broad banded, with a dominant peak at the vortex shedding frequency. In the cases with $Re = 200$ and 250, a secondary peak at half of the shedding frequency was observed in the spectrum of the x and y velocity at points located in the near wake of the downstream cylinder, but this peak was not observed further downstream and it was absent from all points monitored in the cases with $Re = 350$. Therefore, we concluded that modes A and B were dominant when the full nonlinear interactions are considered, and this was confirmed by looking at the evolution of the vorticity iso-surfaces in two shedding cycles, as no mode C structures could be observed. The same behaviour was observed in the flow around bluff rings (Sheard *et al.* 2005*b*).

5. Conclusion

Results have been presented from direct numerical simulations and Floquet stability analysis of the flow around two circular cylinders in staggered arrangements. It was not possible to carry out a Floquet stability analysis for the configuration with $L_y/D = 1.5$, since the flow around this configuration was in the transition range between two vortex-shedding regimes for all Reynolds numbers tested and, consequently, the two-dimensional base flows were not periodic. For all other configurations investigated, we have identified the different modes that take part in the wake transition, using plots of the Floquet multiplier versus spanwise wavenumber and neutral stability curves. With the help of vorticity contours, we have characterized

the symmetries and periodicity of these modes. In addition, the nonlinear behaviour of mode C has been investigated utilizing three-dimensional simulations.

The basic modes in the wake transition in the flow around a single circular cylinder, modes A and B, were also found in the staggered arrangements considered in this investigation. This enforces the thesis that these modes are fundamental in the transition to turbulence in vortex street wakes, even in the case of multiple cylinders. However, one important distinction between the staggered arrangements and the single-cylinder case regarding modes A and B was the different critical Reynolds numbers and corresponding perturbation wavelengths. Both modes originated in the near wake of the upstream cylinder and for all arrangements investigated in the present work, the flow in this region is very similar to that observed in the near wake of an isolated cylinder. This indicates that the physical mechanisms responsible for the manifestation of modes A and B should be the same as in the single-cylinder case.

Another important finding of this study was the presence of mode C in the wake transition for some asymmetrical arrangements. The linear stability results for this mode agree well with previous investigations (Sheard *et al.* 2003; Zhang *et al.* 1995) in many aspects, such as type of perturbation symmetry, wavelength and periodicity. Interestingly, while modes A and B first appear in the near wake of the upstream cylinder, mode C is initiated in the near wake of the downstream cylinder.

The non-linear analysis also produced some interesting results. Mode C bifurcation was subcritical for $L_y/D = 1.0$, supercritical for $L_y/D = 2.0$ and 2.5 and again subcritical for $L_y/D = 3.0$. However, since the vortex shedding regime for $L_y/D = 1.0$ is different from that for $L_y/D \geqslant 2.0$, the configuration $L_y/D = 1.0$ must be considered separately if we want to isolate the three-dimensional effects.

For configurations $L_y/D = 2.0$ and 2.5 mode C presented a supercritical character, but it bifurcated before mode A for $L_y/D = 2.0$ and after mode A for $L_y/D = 2.5$. For $L_y/D = 3.0$, it bifurcated after mode A, but through a subcritical route. Bearing this in mind, we deduce that the character of the bifurcation of mode C is not directly related to the order in which the modes bifurcate.

For $L_y/D \geqslant 1.0$, all three modes appear in the Reynolds number range investigated, and the fact that mode C appears for two substantially different types of wakes ($L_y/D = 1.0$ and $L_y/D \geqslant 2.0$) indicates that the vortex shedding regime and the presence of mode C are not directly related, although both depend on the geometrical configuration of the bodies. In addition, the results presented in this work corroborate the hypothesis that mode C is a fundamental mode in the secondary instability of time-periodic wakes which lose their $\mathscr{H}$ symmetry due to a perturbation imposed by an external agent; in the present case, the external agent was the wake of the upstream cylinder, in Sheard *et al.* (2003) it was the opposite side of the bluff ring and in Zhang *et al.* (1995) the control wire placed close to the cylinder. Mode C seems to replace the quasi-periodic mode that emerges in $\mathscr{H}$-symmetric wakes (Blackburn & Lopez 2003; Marques *et al.* 2004; Blackburn *et al.* 2005), spanning the same wavenumber range.

B. S. C. wishes to acknowledge CAPES-Brazil for financial support during his PhD at Imperial College London and to Hilary Glasman-Deal at ELSP-IG for advice regarding the English language. S. J. S. would like to acknowledge financial support under an EPSRC advanced research fellowship. Computing resources were provided by HPC facilities at Imperial College London and in conjunction with the UK Turbulence Consortium.

Appendix. Calculation of the Floquet multipliers and modes

To calculate the Floquet modes, an operator representing the evolution of the system in one period was constructed:

$$\boldsymbol{u}'_{n+1} = \boldsymbol{A}(\boldsymbol{U})\boldsymbol{u}'_n, \tag{A 1}$$

where $\boldsymbol{u}'_n = \boldsymbol{u}'(x, y, z, t_0 + nT)$ was the perturbation vector after n periods. The eigenvalues of $\boldsymbol{A}$ are the Floquet multipliers of $\boldsymbol{L}$ and the eigenfunctions of $\boldsymbol{A}$ are the Floquet modes at some instant in time t_0, where t_0 depends on the initial phase of the base flow $\boldsymbol{U}$ used to construct $\boldsymbol{A}$.

The action of operator $\boldsymbol{A}$ on the perturbation $\boldsymbol{u}'$ was computed by integrating the linearized Navier–Stokes equations, using the same schemes that were used to compute the base flow. Two changes were necessary in the integration algorithm. The first was that a linear operator $(-(\boldsymbol{U}\cdot\nabla)\boldsymbol{u}' - (\boldsymbol{u}'\cdot\nabla)\boldsymbol{U})$ had to be used to calculate the advection terms. In this operator, the values of $\boldsymbol{U}$ were computed by means of a Fourier interpolation of the time slices resulting from the base flow calculation. The second change was to replace the operator ∇ by $(\partial/\partial x, \partial/\partial y, -\mathrm{i}\beta)$, and compute the three velocity components $(\hat{u}, \hat{v}, \hat{w})$ and $\hat{p}$ on the two-dimensional domains.

The Arnoldi method was used to compute the Floquet multipliers of largest magnitude. We briefly describe this method here; for a more complete discussion the reader should refer to Saad (1992). Essentially, this is an orthogonal projection method of a matrix $\boldsymbol{A}$ onto a k-dimensional Krylov subspace $\mathscr{K}_k \equiv \mathrm{span}\{\boldsymbol{u}, \boldsymbol{A}\boldsymbol{u}, \boldsymbol{A}^2\boldsymbol{u}, \ldots, \boldsymbol{A}^{k-1}\boldsymbol{u}\}$. Given an orthonormal basis $\boldsymbol{Q}_k = [\boldsymbol{v}_0|\boldsymbol{v}_1|\ldots|\boldsymbol{v}_{k-1}]$ of the Krylov subspace $\mathscr{K}_k$, it is possible to decompose the matrix $\boldsymbol{A}$ in the following way:

$$\boldsymbol{A}\boldsymbol{Q}_k = \boldsymbol{Q}_k\boldsymbol{H}_k + h_{k,k-1}\boldsymbol{v}_k\boldsymbol{e}_{k-1}^H. \tag{A 2}$$

$\boldsymbol{H}_k$ is a Hessenberg matrix, whose component on row i and column j is denoted as $h_{i,j}$, $\boldsymbol{v}_k$ is a unitary vector orthogonal to the basis $\boldsymbol{Q}_k$ and $\boldsymbol{e}_{k-1}$ is a unitary vector pointing in the direction of the $k-1$ component. Multiplying both sides of (A 2) on the left by $\boldsymbol{Q}_k^H$ and using the fact that $\boldsymbol{Q}_k$ is orthonormal results in

$$\boldsymbol{Q}_k^H\boldsymbol{A}\boldsymbol{Q}_k = \boldsymbol{H}_k. \tag{A 3}$$

The eigenvalues $\lambda_i^{(k)}$ of the Hessenberg matrix $\boldsymbol{H}_k$ are approximations of the eigenvalues of the matrix $\boldsymbol{A}$, and the approximate eigenvector of $\boldsymbol{A}$ associated with $\lambda_i^{(k)}$, also called the Ritz eigenvector, can be calculated using the expression

$$\boldsymbol{w}_i^{(k)} = \boldsymbol{Q}_k\boldsymbol{y}_i^k, \tag{A 4}$$

where $\boldsymbol{y}_i^k$ is the eigenvector of $\boldsymbol{H}_k$ associated with the eigenvalue $\lambda_i^{(k)}$. Some of the Ritz eigenvalues are good approximations of the eigenvalues of $\boldsymbol{A}$ and the quality of the approximation normally improves as k increases. An efficient way of estimating the residual norm ϵ_i of the approximations is to use the expression

$$\epsilon_i = h_{k,k-1}\left|\hat{\boldsymbol{e}}_{k-1}^H\boldsymbol{y}_i^{(k-1)}\right|. \tag{A 5}$$

An in-house implementation of a restarted Arnoldi algorithm was used to compute the Floquet multipliers of largest magnitude. First, given a first perturbation vector $\boldsymbol{u}'_0$ and using expression (A 1), a Krylov subspace $\boldsymbol{T}_{k+1}$ of dimension $k+1$ was generated:

$$\boldsymbol{T}_{k+1} = \{\boldsymbol{u}'_0, \boldsymbol{u}'_1, \boldsymbol{u}'_2, \ldots, \boldsymbol{u}'_k\}.$$

Next, a QR factorization for the matrix $\boldsymbol{T}_{k+1}$ was calculated, using the modified Gram–Schmidt procedure, as presented in Golub & Van Loan (1996).

With the orthonormal basis $\boldsymbol{Q}_{k+1}$ for the Krylov subspace and the upper triangular matrix $\boldsymbol{R}_{k+1}$ ($\boldsymbol{T}_{k+1} = \boldsymbol{Q}_{k+1}\boldsymbol{R}_{k+1}$), it is possible to derive a simple expression to calculate the Hessenberg matrix $\boldsymbol{H}_k$ correspondent to a k-dimensional Krylov subspace $\mathscr{K}_k = \text{span}\{\boldsymbol{u}'_0, \boldsymbol{u}'_1, \ldots, \boldsymbol{u}'_{k-1}\}$. First, we multiply both sides of (A 3) on the right by $\boldsymbol{R}_k$, and obtain

$$\boldsymbol{Q}_k^H \boldsymbol{A}\boldsymbol{T}_k = \boldsymbol{H}_k \boldsymbol{R}_k. \tag{A 6}$$

Since $\boldsymbol{T}_k$ is generated by the Krylov sequence $\{\boldsymbol{u}'_0, \boldsymbol{A}\boldsymbol{u}'_0, \boldsymbol{A}^2\boldsymbol{u}'_0, \ldots, \boldsymbol{A}^{k-1}\boldsymbol{u}'_0\}$, we can perform the decomposition

$$\boldsymbol{A}\boldsymbol{T}_k = \boldsymbol{Q}_{k+1}\bar{\boldsymbol{R}}_k^{(k+1)}, \tag{A 7}$$

where $\bar{\boldsymbol{R}}_k^{(k+1)}$ is a $(k+1)\times k$ matrix composed of the k last columns of $\boldsymbol{R}_{k+1}$. Substituting (A 7) into (A 6), we obtain

$$\boldsymbol{Q}_k^H \boldsymbol{Q}_{k+1}\bar{\boldsymbol{R}}_k^{(k+1)} = \boldsymbol{H}_k \boldsymbol{R}_k. \tag{A 8}$$

Because the vectors that form the $\boldsymbol{Q}$ matrices are orthogonal, the left-hand side of (A 8) can be written

$$\boldsymbol{Q}_k^H \boldsymbol{Q}_{k+1}\bar{\boldsymbol{R}}_k^{(k+1)} = [\boldsymbol{I}_k|\boldsymbol{0}]\bar{\boldsymbol{R}}_k^{(k+1)} = \check{\boldsymbol{R}}_k^{(k+1)},$$

so $\check{\boldsymbol{R}}_k^{(k+1)}$ is a $k\times k$ matrix made up of the last k columns and first k lines of matrix $\boldsymbol{R}_{k+1}$. Using the fact that both $\check{\boldsymbol{R}}_k^{(k+1)}$ and $\boldsymbol{R}_k$ are submatrices of $\boldsymbol{R}_{k+1}$, the final expression, $\check{\boldsymbol{R}}_k^{(k+1)} = \boldsymbol{H}_k \boldsymbol{R}_k$, can be written in index form ($r_{i,j}$ and $h_{i,j}$ are elements on row i and column j of the matrices $\boldsymbol{R}_{k+1}$ and $\boldsymbol{H}_k$ respectively):

$$r_{i,j+1} = \sum_{l=0}^{j} h_{i,l} r_{l,j},$$

which can be rearranged in order to give the values of the matrix $\boldsymbol{H}_k$:

$$h_{i,j} = \frac{1}{r_{j,j}}\left(r_{i,j+1} - \sum_{l=0}^{j-1} h_{i,l} r_{l,j}\right). \tag{A 9}$$

Therefore, to resume the description of the implementation, after doing a QR factorization for the matrix $\boldsymbol{T}_{k+1}$, the matrix $\boldsymbol{H}_k$ was calculated using (A 9). The eigenvalues and eigenvectors of $\boldsymbol{H}_k$ were calculated using the LAPACK routines (Anderson *et al.* 1999), and the residual was estimated using (A 5).

In practice, a maximum value for the dimension of the Krylov subspace was specified, and the actual k started with 1. In every iteration the value of k was incremented, the Krylov subspace was updated, the calculations were carried out and the residual was calculated. If the Krylov subspace dimension reached the specified maximum size before convergence, a new vector in the Krylov sequence was generated and the oldest vector was discarded, thus keeping the Krylov subspace size constant and equal to the maximum size specified. This is equivalent to restarting the method with the second oldest vector in the sequence. Once the required eigenvalues had converged, the Ritz approximations of the correspondent eigenvectors of $\boldsymbol{A}$ were computed using (A 4). If the converged Floquet multiplier was a complex pair, the Ritz eigenvectors were calculated using the same approach as the LAPACK routines (Anderson *et al.* 1999), using one vector for the real part and one for the imaginary part, thus making it possible to fully reconstruct the Floquet mode.

This implementation has the advantage of providing an explicit restart without the disadvantage of resetting the size of the Krylov subspace to 1 again, as in the method presented by Saad (1992). Compared to Implicit Restarted Arnoldi methods (Lehoucq & Sorensen 2000), the method presented here is easier to implement. The calculation of the action of the operator $\boldsymbol{A}(\boldsymbol{U})$ over the perturbation, which was actually an integration in time, was much more expensive than the QR decomposition of the matrix $\boldsymbol{T}_{k+1}$; therefore the fact that the decomposition must be made in every iteration was not a significant drawback when considering the total computational time.

REFERENCES

Akbari, M. H. & Price, S. J. 2005 Numerical investigation of flow patterns for staggered cylinder pairs in cross-flow. *J. Fluids Struct.* **20**, 533–554.

Anderson, E., Bai, Z., Bischof, C., Blackford, S., Demmel, J., Dongarra, J., Du Croz, J., Greenbaum, A., Hammarling, S., McKenney, A. & Sorensen, D. 1999 *LAPACK Users' Guide*, 3rd edn. SIAM.

Barkley, D. & Henderson, R. D. 1996 Three-dimensional Floquet stability analysis of the wake of a circular cylinder. *J. Fluid Mech.* **322**, 215–241.

Blackburn, H. M. & Lopez, J. M. 2003 On three-dimensional quasiperiodic Floquet instabilities of two-dimensional bluff body wakes. *Phys. Fluids* **15**, 57–60.

Blackburn, H. M., Marques, F. & Lopez, J. M. 2005 Symmetry breaking of two-dimensional time-periodic wakes. *J. Fluid Mech.* **522**, 395–411.

Carmo, B. S. 2005 Numerical investigation of the flow around two cylinders in tandem arrangements. Msc dissertation, Escola Politécnica – University of São Paulo, Brazil.

Dušek, J., Le Gal, P. & Fraunié, P. 1994 A numerical and theoretical study of the first Hopf bifurcation in a cylinder wake. *J. Fluid Mech.* **264**, 59–80.

Gerrard, J. H. 1966 The mechanics of the formation region of vortices behind bluff bodies. *J. Fluid Mech.* **25**, 401–443.

Golub, G. H. & Van Loan, C. F. 1996 *Matrix Computations*, 3rd edn. Johns Hopkins University Press.

Henderson, R. D. 1997 Nonlinear dynamics and pattern formation in turbulent wake transition. *J. Fluid Mech.* **352**, 65–112.

Henderson, R. D. & Barkley, D. 1996 Secondary instability of the wake of a circular cylinder. *Phys. Fluids* **8**, 1683–1685.

Karniadakis, G. E. 1990 Spectral Element–Fourier methods for incompressible turbulent flows. *Comput. Meth. Appl. Mech. Engng* **80**, 367–380.

Karniadakis, G. E., Israeli, M. & Orszag, S. A. 1991 High-order splitting methods for the incompressible Navier–Stokes equations. *J. Comput. Phys.* **97**, 414–443.

Karniadakis, G. E. & Sherwin, S. J. 2005 *Spectral/hp Element Methods for Computational Fluid Dynamics*, 2nd edn. Oxford University Press.

Lehoucq, R. B. & Sorensen, D. C. 2000 Implicit restarted Arnoldi method (section 7.6). In *Templates for the Solution of Algebraic Eigenvalue Problems: A Practical Guide* (ed. Z. Bai, J. Demmel, J. Dongarra, A. Ruhe & H. van der Vorst), pp. 166–185. SIAM.

Leweke, T. & Williamson, C. H. K. 1998 Three-dimensional instabilities in wake transition. *Eur. J. Mech.* B/*Fluids* **17**, 571–586.

Marques, F., Lopez, J. M. & Blackburn, H. M. 2004 Bifurcations in systems with Z2 spatio-temporal and O(2) spatial symmetry. *Physica* D **189**, 247–276.

Mizushima, J. & Suehiro, N. 2005 Instability and transition of flow past two tandem circular cylinders. *Phys. Fluids* **17**, 104107.

Noack, B. R. & Eckelmann, H. 1994 A global stability analysis of the steady and periodic cylinder wake. *J. Fluid Mech.* **270**, 297–330.

Persillon, H. & Braza, M. 1998 Physical analysis of the tansition to turbulence in the wake of a circular cylinder by three-dimensional navier-stokes simulation. *J. Fluid Mech.* **365**, 23–88.

Posdziech, O. & Grundmann, R. 2001 Numerical simulation of the flow around an infinitely long circular cylinder in the transition regime. *Theore. Computat. Fluid Dyn.* **15**, 121–141.

Provansal, M., Mathis, C. & Boyer, L. 1987 Bérnard-von Kármán instability: transient and forced regimes. *J. Fluid Mech.* **182**, 1–22.

Robichaux, J., Balachandar, S. & Vanka, S. P. 1999 Three-dimensional Floquet instability of the wake of a square cylinder. *Phys. Fluids* **11**, 560–578.

Saad, Y. 1992 *Numerical Methods for Large Eigenvalue Problems*. Manchester University Press.

Sheard, G. J., Thompson, M. C. & Hourigan, K. 2003 From spheres to circular cylinders: the stability and flow structures of bluff ring wakes. *J. Fluid Mech.* **492**, 147–180.

Sheard, G. J., Thompson, M. C. & Hourigan, K. 2004 From spheres to circular cylinders: non-axisymmetric transitions in the flow past rings. *J. Fluid Mech.* **506**, 45–78.

Sheard, G. J., Thompson, M. C. & Hourigan, K. 2005*a* Subharmonic mechanism of the mode C instability. *Phys. Fluids* **17**, 111702.

Sheard, G. J., Thompson, M. C., Hourigan, K. & Leweke, T. 2005*b* The evolution of a subharmonic mode in a vortex street. *J. Fluid Mech.* **534**, 23–38.

Sumner, D., Price, S. J. & Païdoussis, M. P. 2000 Flow-pattern identification for two staggered circular cylinders in cross-flow. *J. Fluid Mech.* **411**, 263–303.

Thompson, M. C., Hourigan, K. & Sheridan, J. 1996 Three-dimensional instabilities in the wake of a circular cylinder. *Exp. Therm. Fluid Sci.* **12**, 190–196.

Thompson, M. C., Leweke, T. & Williamson, C. H. K. 2001 The physical mechanism of transition in bluff body wakes. *J. Fluids Struct.* **15**, 607–616.

Williamson, C. H. K. 1988 The existence of two stages in the transition to three-dimensionality of a cylinder wake. *Phys. Fluids* **31**, 3165–3168.

Williamson, C. H. K. 1996 Three-dimensional wake transition. *J. Fluid Mech.* **328**, 345–407.

Wu, J., Sheridan, J., Welsh, M. C., Hourigan, K. & Thompson, M. C. 1994 Longitudinal vortex structures in a cylinder wake. *Phys. Fluids* **6**, 2883–2885.

Zdravkovich, M. M. 1972 Smoke observations of wakes of tandem cylinders at low reynolds numbers. *Aero. J.* **76**, 108–114.

Zdravkovich, M. M. 1977 Review of flow interference between two circular cylinders in various arrangements. *Trans. ASME: J. Fluids Engng* **99**, 618–633.

Zhang, H.-Q., Fey, U., Noack, B. R., König, M. & Eckelmann, H. 1995 On the transition of the cylinder wake. *Phys. Fluids* **7**, 779–794.